Three-Dimensional (3D) Velocity Map Imaging: From Technique to Application

Gihan Basnayake, Yasashri Ranathunga, Suk Kyoung Lee and Wen Li*

Department of Chemistry, Wayne State University, Detroit, Michigan, 48202, USA

*Corresponding author: wli@chem.wayne.edu

Abstract

The velocity map imaging (VMI) technique was first introduced by Eppink and Parker in 1997, as an improvement to the original ion imaging method by Houston and Chandler in 1987. The method has gained huge popularity over the past two decades and has become a standard tool for measuring high-resolution translational energy and angular distributions of ions and electrons. VMI has evolved gradually from 2D momentum measurements to 3D measurements with various implementations and configurations. The most recent advancement has brought unprecedented 3D performance to the technique in terms of resolutions (both spatial and temporal), multi-hit capability as well as acquisition speed while maintaining many attractive attributes afforded by conventional VMI such as being simple, cost-effective, visually appealing and versatile. In this tutorial we will discuss many technical aspects of the recent advancement and its application in probing correlated chemical dynamics.

Key Words: 3D VMI, coincidence imaging, multielectron dynamics, 3D momentum imaging

1. Introduction

The complete kinematic information of a physical or chemical process, in which particles (ions/neutrals/electrons) are released, is critically important and revealing for studying its detailed dynamics. This is because the energetics of these particles as well as their angular distributions reflect the intimate details of the potential energy surfaces, on which these dynamics take place. These processes include chemical reactions initiated by collisions (between photons and molecules or between molecules), high energy particle collisions and surface dynamics induced by photon/particle impact. The resulting fragments in these collision processes scatter in various directions and expand as a series of concentric spheres or hemispheres (from a surface). These spheres are known as Newton spheres, and each can have its own chemical and quantum state identity. Fully characterizing these spheres in momentum space and the correlation among different spheres provide a powerful tool to understand the dynamics that produce them. Considering the universality of the phenomena, it is not surprising that quite a few scientific communities have been actively developing 3D momentum imaging techniques. To name a few: high energy physics, atomic, molecular, and optical (AMO) physics, chemical dynamics and material/surface dynamics. VMI's origin sat squarely within the chemical dynamics community and its need for an easier implementation of the more primitive methods such as photofragment translational spectroscopy (PTS)[1-4] and laser based Doppler techniques[5-7], which essentially recorded one-dimensional projection of the 3D Newton spheres. Over the two decades from 1970s to 1990s these techniques dominated the photodissociation studies until the groundbreaking work of Chandler and Houston in 1987[8], in which a 2D imaging detector was employed to record a 2D projection of the Newton sphere for the first time. Eppink and Parker[9] developed VMI in 1997 by replacing a homogenous electric field for accelerating ions/electrons with an inhomogeneous electric field that can focus particle trajectories according to their momenta. It is interesting to note, around the same time, the AMO physics community started developing the so-called cold target recoil ion momentum spectroscopy (COLTRIMS) by combining

a homogenous extraction field and an advanced 3D imaging detector based on delay-line techniques[10]. In the past two decades, VMI has kept evolving. In 2001, pulsed slice ion imaging was developed by Kitsopoulos and co-workers to extract center slices of Newton spheres[11]. In 2003, direct current (DC) slice ion imaging was developed by Suits and co-workers[12] and Liu and co-workers[13]. In 2000, delay-line detectors were introduced into a VMI spectrometer to achieve direct 3D momentum measurements by Eland and co-workers[14]. During this period, VMI started gaining popularity in the AMO physics community and many different spectrometer designs have been explored. In 2014, our group at WSU developed a new version of 3D-VMI which utilized a conventional VMI setup with just a few additional parts[15-17]. This setup achieved direct 3D measurements of both electrons and ions with a simple implementation of a position- and time- sensitive detector. Since then, the performance of the system has improved significantly and now it has rivaled or surpassed those of a delay-line detector. This tutorial will focus mainly on this new detection system and its application in probing chemical dynamics as well as providing a brief review of relevant prior techniques.

2. Capturing the Newton sphere - from crush, slice to 3D

In its conventional form (Fig. 1), the velocity map imaging spectrometer projects the three-dimensional Newton sphere onto a two-dimensional imaging detector to form a projection or “crushed” image sometime referred to as a Newton pancake. The size of the 2D-image is a direct reflection of the speed of fragments while its shape represents the angular distribution. There are a few numerical methods that can be used to recover the underlying 3D velocity distribution from this 2D crushed image (Fig. 2). The most-commonly used methods are based on the inverse Abel transform[18, 19] and this requires the original system to be cylindrically symmetric with the symmetry axis lying along the detector plane. Most of the systems that are used in photodissociation studies in VMI under linearly polarized light produce a cylindrically symmetric fragment scattering distribution along the polarization axis and from direct mapping, the 3D distribution is recovered by Abel inversion. However, the inverse Abel transform can introduce noise along the symmetry axis and become unstable. Numerous approaches have been developed to address these issues and to improve the accuracy of reconstruction of the 3D distribution. Among these methods, the iterative reconstruction method[20], back projection onion peeling method[21], and the Basis Set Expansion or BASEX[22] method are proven to be efficient and produce noise free reconstruction and the BASEX method has been popular due to its efficiency and accuracy[23]. An variant of BASEX known as pBASEX was introduced by Powis and co-workers[24] that depends on fewer number of parameters to improve the signal to noise ratio. Several other approaches[25-27] with excellent performance have emerged over the years, some of which can retrieve 3D distributions from 2D images even without a cylindrical symmetry[28].

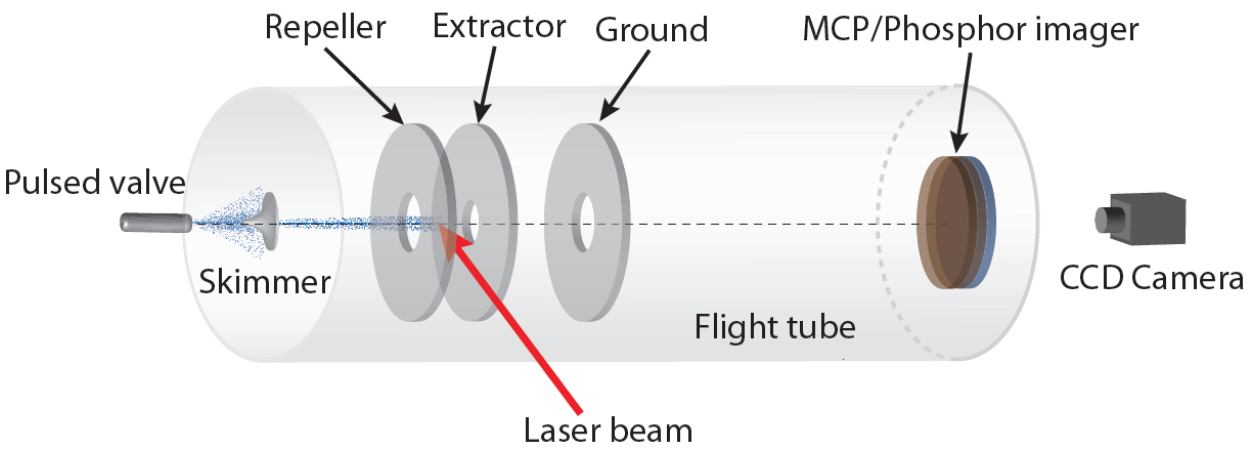

Fig. 1 A typical 2D-VMI setup. The repeller, the extractor, the ground electrodes and the flight tube form a spectrometer while the imaging detector and the camera make the detection system.

Although the image reconstruction methods discussed above offer an efficient analytical reconstruction, they cannot be considered as completely noise free methods. In some cases, apart from noise they could introduce artifacts into the reconstructed images making some regions unworkable. These methods work only on the systems with cylindrical symmetry and for the systems that produce the photofragment distribution without the cylindrical symmetry or investigating into the low velocity distributed regions, a different method is required. For this purpose, a few techniques have been introduced to either capture the full three-dimensional Newton sphere or a finite slice without the use of image reconstruction methods.

Slice imaging is such a technique that directly captures a finite slice of the Newton sphere along the time-of-flight axis, circumventing the need for an image reconstruction. This was first introduced by Kitsopoulos and co-workers[11] in 2001 using delayed extraction fields. In 2003 Townsend et al.[12] and Lin et al. [13] developed a new approach with an increased resolution known as DC sliced imaging which has become the most popular among the slice imaging methods[29-31]. In all slice imaging approaches, Newton spheres are not “pancaked” as much as in conventional VMI and are allowed to stretch along the TOF axis so that the detector can be gated (a few tens of nanoseconds) to capture the center slice. Due to a finite and flat time slice (partial slicing), residual blurring and a non-uniform collection efficiency of fragments with different kinetic energies[32] pose some issues when quantitatively extracting data. Suits and co-workers developed numerical methods (FinA) to address these issues and achieved outstanding results[33, 34].

Slice imaging, though it captures the three-dimensional distribution without the need of image reconstruction, cannot be considered as a suitable technique for coincidence imaging where the complete measurement of all three-dimensional momenta of the product fragments is required to determine the complete kinematic picture of the event. It feasible to measure the complete three-dimensional distribution by shifting detector gate along the time-of-flight distributions to record a series of slices through the Newton sphere. However, this is a slow and tedious process and significant distortions in the measured three-dimensional distributions can be introduced because of the experimental drifts over the time[35].

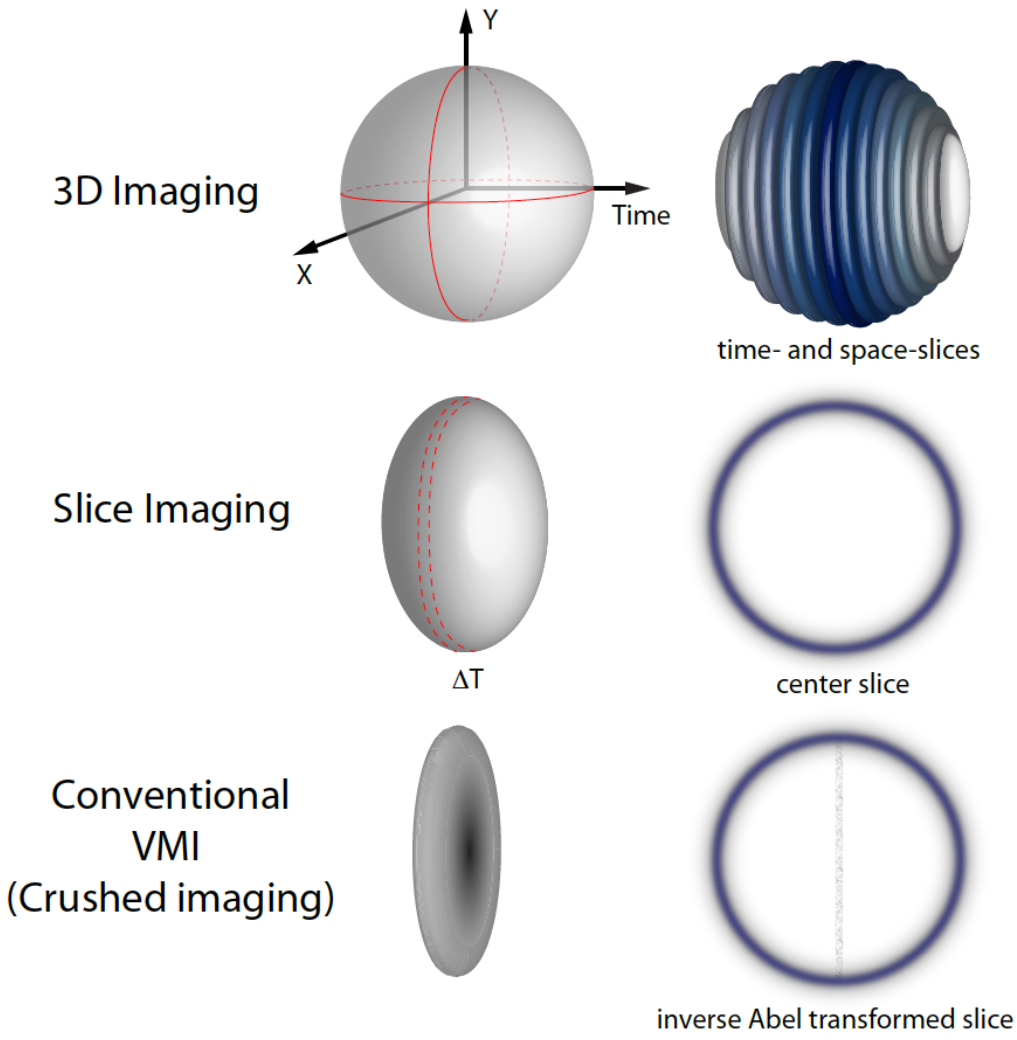

Fig. 2 An illustration of Crush, Slice, and 3D imaging

As a more direct method to capture the complete 3D momentum distributions, simultaneous measurement of the position and time of fragments with a fast detector can be used. For this purpose, a microchannel plate (MCP) stack and anode based readout devices such as a delay line[36] or a camera-based system utilizing the fast decay characteristics of a phosphor screen[37] were employed. More commonly, such 3D detectors have been applied with spectrometer designs featuring a homogenous electric field[38, 39]. These setups usually achieve inferior energy resolution compared to a 2D VMI setup.

3. 3D detectors– technical considerations and prior implementations

In a TOF-based momentum imaging system, the two essential components are the spectrometer and the detector. The spectrometers provide various electrostatic potentials to accelerate charged particles out of interaction region toward the detectors, which register the position coordinates and/or time of flight. In the past three decades, there have been significant amount of work dedicated to designing suitable spectrometers to use in different applications. The readers are referred to a few excellent comprehensive reviews on the topic[40, 41]. In this tutorial, all work employed a standard DC slice imaging spectrometer featuring 4 or 5 electrodes to provide a velocity focusing electric fields while allowing enough TOF

separation to achieve 3D measurements. Below, we will briefly review various relevant detection schemes before moving on to the more recent development.

A typical detector assembly is composed of a gain amplification stage and a readout anode. The most common amplification device is a microchannel plate (MCP) even though in-vacuum pixel detectors based on Medipix and Timepix[42] has been recently demonstrated without MCPs[43-45]. The introduction of MCPs in early 1970s can be considered as the real beginning of imaging techniques[46]. An MCP is a flat lead glass disc with a typical thickness of 1-2 mm and the maximum outer diameter of about 150 mm. In an MCP there are millions of thin channels that have the pore size of a few tens of μm or 2 μm in highest resolution MCPs. Low spacing (3- 32 μm) between the channels provides a high spatial resolution. They also feature high time resolution that depends on the pore size (smaller pore size produces better time resolution) and high gain ($\sim 10^4$ for a single plate). For a higher gain, an assembly of MCPs is made from several stacked MCPs and the most common assemblies are Chevron dual plate assembly and Z-stack triple plate assembly. These assemblies provide higher gain and can be operated at higher voltages (Chevron: 2000 V typical, 10^6 - 10^7 gain and Z- configuration 3000 V typical, 10^7 -10^8 gain). The channel pores on MCPs are positioned with a small bias angle to prevent the ion feedback and this also reduces penetration of particles deeply into the channels when they fly parallel to the axes of the channels which reduces the production of secondary electrons and in turn reducing the total gain[46].

After the MCP, many types of readout devices have been used to detect the electron avalanche resulting from the impact of ions and electrons. In mass spectrometry where position information is not required a single metal anode is used for detection and counting particles. The requirement changes when it comes to imaging where a time and position sensitive detector is required. There are many read-out schemes that can capture the spatial and temporal information coming from the electric output signal of MCPs. These readout techniques were initially developed and have been used in space-and nuclear based applications such as photon counting[44, 47] and later they were adopted into chemical imaging and led to the 3D momentum imaging techniques. The read-out techniques mainly used in chemical imaging can generally be divided into two types: that are based on combined MCP- electronic readouts and that are based on MCP- scintillator coupled with pixelated silicon sensors (or optical readouts).

For the first type, there are a few major schemes that have been extensively used in chemical imaging. As a result of developing a photon detection technique, the wedge and strip anode systems provide an effective and simple two-dimensional position sensitive detection method[48, 49]. Generally, it is composed of three or four independent electrodes and can be used in different arrangements[50]. One of the commonly used anodes consists of three coplanar anodes called wedge, strip, and meander according to their shape. The detector is placed behind the MCPs and when an electron cloud from the back of MCP hits the anode the charge is distributed over the three electrodes. The point of detection can be measured by measuring the charge on each anode independently. They offer a very good position resolution but fails when it comes to detection of multi-hits. Another approach which offers a good temporal resolution is the crossed wire detectors[51, 52]. They consist of two independent insulated wire sets along x and y axes. The wires are positioned equally spaced and perpendicular to each other and the signal from each wire is processed independently when an electron cloud hits a crossing of two wires and thus the position and the time of the event are determined. This technique also fails to detect multiple particles simultaneously and the position resolution is largely limited by the need of readout electronics for the number of anodes, and the spacing of wires in the detector. Technically realized in early 1990s by Eland[53, 54], the delay line detectors (DLDs) have been a more popular MCP-anode readout technique in 3D and coincidence imaging due to their high spatial and temporal resolution, and short dead time[39,

55-58]. The technique has been widely used as a part of the COLTRIM technique or 3D ion imaging. DLDs in their simplest form are composed of two individual wound anodes orthogonal to each other. When the electron cloud from the MCPs hits a delay line wire pair, the electric signal induced in the wires propagates to the ends where it is amplified by a differential amplifier and recorded. Combination with fast time to digital converters (TDCs) enables DLDs to be used in large-frequency applications with highly accurate temporal and spatial information[59, 60]. Although the original form is very restrictive in multi-hit detection, the hexanode versions in which three delay lines are wound in a hexagonal geometry have achieved good multi-hit capability with a deadtime around 5 ns[61].

The second type of readout is based on luminescence detection from a scintillator screen and has a good multi-hit capability. These phosphor screens are generally coupled with pixelated silicon devices (cameras). Numerous phosphor screen and camera-based imaging systems have been developed over the past few decades and the detection efficiency and multi-hit capability have been improved greatly. Chandler and Houston's work can be considered as the beginning of this concept, today known as the photofragment imaging technique. They employed a combination of time of flight mass spectrometry and microchannel plates for charged particle detection and the addition of a fluorescent screen to see the fragments from photolysis of methyl iodide[62]. In their first experiment, the phosphor screen was captured by a polaroid camera film as the image was clearly visible to the naked eye and the image was then digitized. Later the system was improved by employing a charge coupled device (CCD) camera. While majority of these experiment collect 2D positional information, there were some prior attempt of 3D imaging using phosphor screens and CCD cameras. Neumark and co-workers[63, 64] incorporated a multi-anode photo-multiplier tube (PMT) along with a CCD camera behind a phosphor screen where a spot is produced by each event based on a scheme employed by Zajfman *et al.*[58]. The spatial information is captured by the CCD camera while the temporal information and rough positional information are obtained from the PMT. The other concept introduced by Zajfman and co-workers, incorporates two CCD cameras focusing on the phosphor screen[65]. Here one camera runs continuously while the other camera is time gated in order to capture the light over a finite time. Using the light intensities from both cameras the time of flight can be retrieved and the multi-hit detection of ions on phosphor is achieved at the same time. There was a limitation in this concept as the time resolution was dependent on the phosphor decay. There was another 3D scheme developed by combining a phosphor screen with a DLD and a CCD camera to allow additional spatial information while the DLD is used to extract precise measurements[59, 66, 67]. Finally, it has now become possible to achieve 3D imaging with specialized cameras based on hybrid pixel detectors. Among these, the Timepix sensor family was originally developed at CERN for applications in detecting both the position and arrival time of high energy particles[42, 68]. It has been adopted in a few visible photon cameras such as PImMS and Timepix3cam [69] [70].

4. A new 3D imaging system: the need for speed

An important feature of 3D momentum imaging techniques is the capability of collecting coincident events. This is somewhat related to the multi-hit capability of the detector. However, multi-hit capability alone is not sufficient. This is because coincidence detection requires a very low event rate (far less than 1 event/laser shot) and thus a high repetition rate is desired in order to accumulate enough statistics in a finite acquisition time. The CCD+PMT method by Zajfman and co-workers was limited by the frame rate of a CCD camera, which was typically less than 100 Hz. Such a setup was not ideal for coincidence measurement.

In 2014, a new approach was developed for fast 3D imaging of ions and electrons by Li and co-workers [15], motivated by the need for speed in coincidence 3D imaging. In comparison to Zajfman's method, this simple design utilizes a high frame rate CMOS camera and a single anode PMT (later MCP pick-off directly) coupled to a high-speed digitizer, which work together with a conventional 2D MCP/phosphor screen imaging detector. The multi-hit capability is achieved by correlating the brightness of electron/ion spots from the camera and the heights of the TOF peaks from the digitizer (Fig. 3). The system is simple, versatile, and high performing in both resolution (spatial and temporal) and multi-hit capability. A similar scheme but with a different hardware implementation was later demonstrated by Urbain et al.[71]. Here we will describe some technical considerations of each essential component of this system in detail.

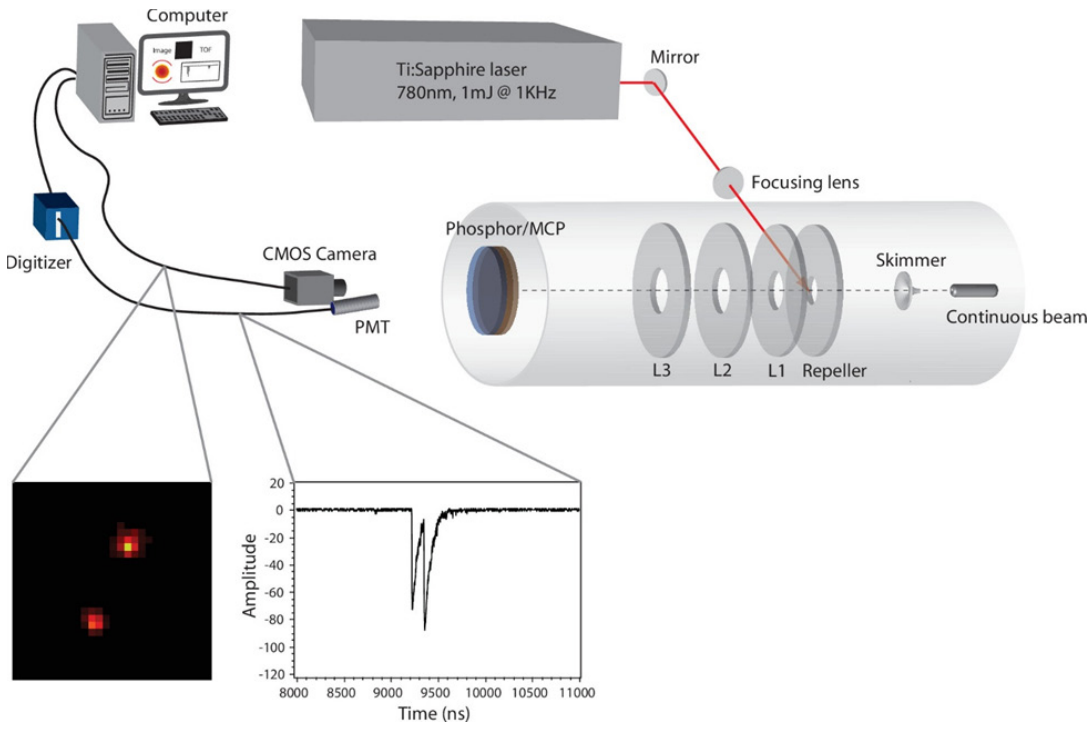

Fig. 3 WSU coincidence ion imaging apparatus. A coincidence event of two ions being detected on the PMT and the CMOS camera is shown. (Reproduced from [15] with the permission from of AIP Publishing)

4.1 High-speed cameras

One of the enabling techniques for the setup is a high-performing CMOS camera. Most of the commercially available CMOS cameras are designed for industrial applications/machine vision. These cameras usually have a high readout noise (higher than 50 electrons/pixel). A rough estimate suggests in a typical VMI setup (with a dual-MCP imaging detector), each pixel in the camera will only see a few hundred of photons. Considering the quantum efficiency of a camera pixel (~50%), this put a stringent requirement on camera's low light performance and renders most of the CMOS cameras on the market unsuitable, even though they can reach a quite high frame rate. With an image intensifier, it might be possible boost the photon budget to allow the usage of these cameras[72]. But this will add cost and

complexity to the system. In 2013, commercial CMOS cameras achieved technical breakthroughs in terms of noise reduction (a few electrons/pixel) while still being able to reach a high frame rate (>1000 frame/s). This improvement has allowed CMOS cameras to directly compete in image quality and eventually edged out CCD cameras in almost all applications. In the past few years, fast and sensitive CMOS cameras have become quite affordable with ever-increasing resolutions. Table 1 lists a few camera models that are suitable in the camera-based 3D VMI setup. It should be noted that these cameras use standard USB3 Vison or GigE Vision interfaces, which are both based on GenICAM (generic interfaces for cameras) software interface. This means that the image acquisition software only needs to be written once and will be compatible with other cameras even from different manufacturers. This has greatly simplified the development of the software package and allow the 3D VMI system to exploit the rapidly evolving technical advancement in machine vision industry.

Table 1. a few CMOS cameras with typical performance parameters

Manufacturer/model	Native resolution (pixel^2)	Resolution at 1K frames/s (pixel^2)	Readout noise (e/pixel)
FLIR/ GS3-U3-23S6M-C[a]	1920×1200	128×128	7
Basler/ acA640-750um[a]	640×480	460×460	9
Basler/acA720-520um[a]	720×540	260×260	4
Emergent Vision/HB-500-S	812×620	812×620 (frame rate ~1600)	3[b]

[a]These cameras have been tested in the Li group.

[b]This number was not directly available in public domain but was estimated from a different SONY CMOS senor (IMX430) manufactured with the same technology.

These CMOS cameras are capable of a few thousand of frames per seconds, which is sufficient to use in coincidence measurement. Exploiting the low event rate of coincidence experiments, it is possible to run the overall repetition rate of the system (limited by the laser) at a much higher rate than the camera frame rate. We demonstrated this using a 2000 frames/s camera with a 10 kHz laser, which boosted the data acquisition speed significantly[73].

To reach an even higher acquisition speed, simply increasing the camera frame rate quickly becomes impractical for two reasons: (1) the cost of such cameras is prohibitively high. (2) the huge amount of data produced at such a high frame rate cannot be streamed continuously to a host computer for processing. Instead, the data can only be stored in internal memory modules, which have limited capacity. This limits the acquisition time to just a few minutes, which is not ideal.

Recently, a solution has been provided for achieving an event rate approaching one million hits per second with the camera-based 3D VMI. The setup featured a new type of event driven cameras (Tpx3cam), that do not record frames but output only non-zero-pixel events with accurate time stamps. This event rate is close to that of a delay-line detector[74].

4.2 PMT or MCP pick-off of timing signals

Initially, the timing information of the ion hits was picked off using a photomultiplier tube pointing at the phosphor screen. We call this an all-optical method (camera+PMT). A PMT with a few nanoseconds rise time was selected to achieve a good time resolution for ion imaging. Because the rise time of the phosphor (P47) is around 4-6 ns, there is no need for even faster PMTs. An RCA 931B PMT was used in our first

demonstration while many more PMT were suitable. Because P47 phosphor has slow decay (100ns), the full waveform does not help achieve a good time resolution. Instead, only the rising edge was used. The dynamic range of the PMT was increased by modifying the resistor chain voltage divider. This helped counteract the space charge saturation effect with the increased voltage of the last three dynodes.

Later on, in order to achieve a very high time resolution for measuring electron TOFs, electric signals from MCPs were picked off directly and sent to the digitizer to extract the TOF of the hits. This was done using a simple capacitive decoupling circuitry. A typical MCP signal has a rise time of 3 ns and a FWHM of 5 ns. In this case, the full waveform can be used to extract TOF and has achieved a remarkable TOF resolution of ~30ps (standard deviation). It should be noted because of the impedance mismatch, the MCP waveforms come with significant ringing. It is very difficult to suppress them completely, unlike in a typical mass spectrometry setup (only TOF) in which a cone-shaped metal anode can be used to match the impedance. A typical optimization is to move the first ringing away from the main signal, so it won't interfere with the main pulse shape.

To completely avoid the ringing issue while still achieving a good TOF resolution, we recently returned to the all-optical approach for electron 3D momentum imaging. However, a dye-based fast scintillator has to be used. A fast silicon photomultiplier (Si-PM) was also adopted. The achieved time resolution was similar to that of MCP pick-off but deadtime was further reduced to an unprecedented 0.48 ns[75].

4.3 High-speed digitizer

The full PMT/MCP waveforms were acquired after each laser shot using a digitizer to extract TOFs. Previously, the most popular approach was to use a time-to-digital converter (TDC) after the signal was first processed by constant fraction discriminators (CFD). CFD was critical for suppressing the timing walk-off issue due to the stochastic nature of the MCP signal. In this configuration, only the leading edge of the signal was utilized, and the achieved resolution was largely dependent on the resolution of a TDC and system jitters. Furthermore, the pulse width should not be too narrow and TDC has a significant deadtime issue (10 ns). We opted to use a high-speed waveform digitizer to avoid these issues and achieved unprecedented performance. Under the oversampling condition, as long as the trigger jitter is suppressed, it has been shown that the digitizer approach can achieve >10$\times$ better time resolution than the sampling period of the digitizer. Two different methods can be used to suppress trigger jitters: 1) Using built-in trigger time interpolator. 2) Digitizing simultaneously the trigger and TOF signal waveforms using two channels on the digitizer or using one channel by combining both signals. The first method is preferred because it is simpler. There are few manufacturers that provide trigger time interpolation with an accuracy of a few picoseconds. These include National Instruments and Acqiris. Another important consideration when selecting a digitizer is its ability to simultaneous acquire and stream waveform data. This is to avoid any gap in data acquisition that the digitizer has to incur to download the data from on-board memory. In the Li lab, a few digitizers have been tested in the past few years. These include PXIe 5162, PXIe5183, PXIe 5114 from National Instruments, ATS9373 from AlazarTech and 1070A from Acqiris. Many other digitizers are certainly suitable and will be tested in the future, if budget allows.

4.4 Data acquisition program

One of the most important components of the camera-based 3D imaging system is a computer program that integrate and synchronize the image and TOF acquisitions. This program processes camera images and extracts TOF information from MCP signals in real time. It is critical that these are done in real time

because the data rate is very high, especially for camera data. For a typical image acquisition at 460 pixels by 460 pixels and 1000 frames/s, the data rate can amount to more than 200 megabytes (MB) per second. It is impractical to save all these data for post-analysis. This requires the program to have time-efficient routines to analyze each image and extract the positions of each event. The Li group developed such a routine based on an advanced centroiding event counting program[76], which calculates the center of mass of clusters of non-zero pixels in each camera frame on-the-fly. The center-of-mass calculation can achieve a sub-pixel spatial resolution. Modifications were added to compute the intensity of each cluster for the purpose of associating multi-hit events. The routine has been tested to run at more than 1000 frames/s for images at 1000 pixels by 1000 pixels and can run much faster at a lower resolution. Furthermore, the acquisition program distributes the data acquisition and data processing to different central processing units (CPUs) cores using a parallel computing algorithm in a multicore CPU desktop. A queue data structure is implemented in Labview as a data buffer. This isolates the data acquisition process from any potential slowdowns in data analysis. This is important because operating systems such as Windows are not real-time systems and unpredictable latency could lead to frame skipping and thus data loss, if not handled properly.

On the TOF side, the program acquires live traces of TOF signals (PMT or MCP) from the digitizer and performs a peak detection algorithm to extract the TOF of each hit in real-time. The peak height can be easily obtained from the waveform to associate multi-hit events. For electrons, because the TOF spread is usually small (less than ten nanoseconds), it is possible to save every waveform in storage devices for post-analysis. With these waveforms, a more advanced and time-consuming nonlinear fitting algorithm can be applied to retrieve more accurate TOFs and to achieve the shortest deadtime when detecting two electrons.

The flowcharts of both acquisition and analysis programs are reproduced below for reference (Fig. 4).

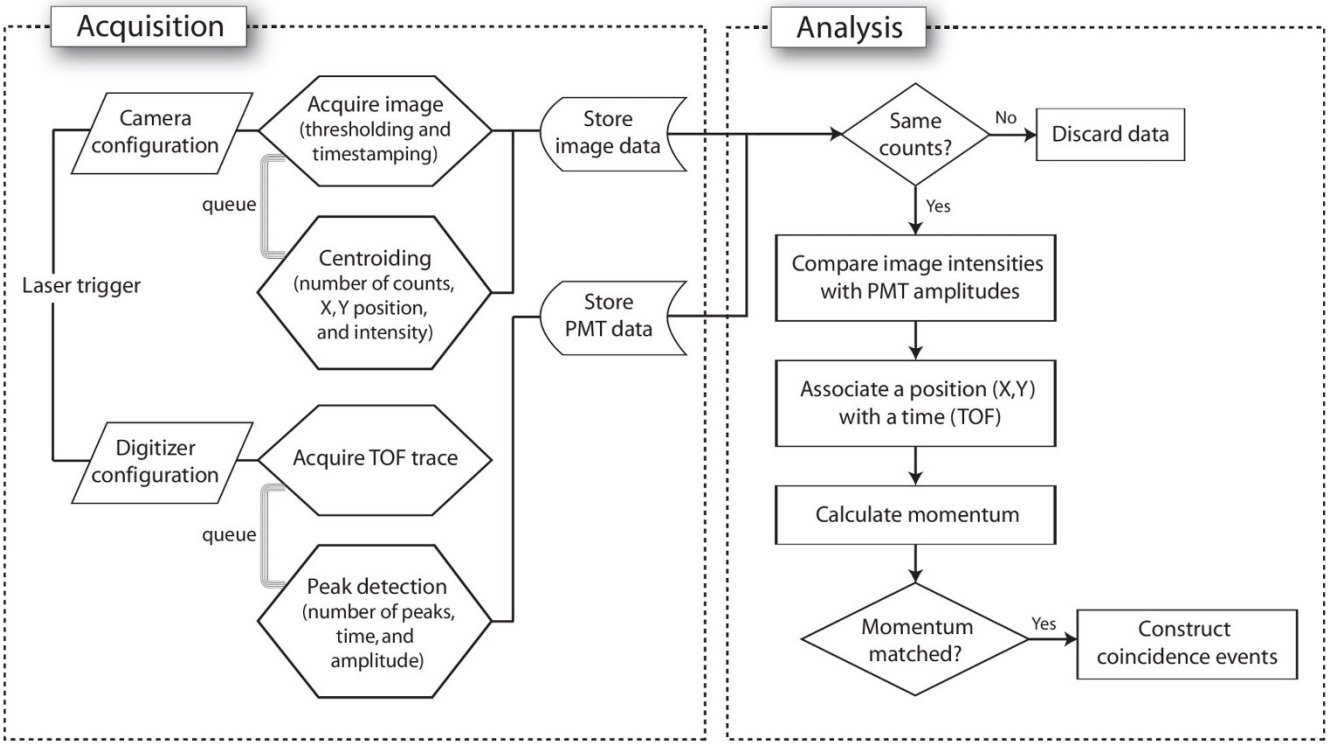

Fig. 4 The flow chart of the 3D-VMI Data Acquisition and Analysis Algorithms. (Reproduced from [15] with the permission from of AIP Publishing)

The synchronization between the camera and the digitizer is done at both hardware and software level (Fig. 5). The laser trigger picked off by a photodiode is used to trigger the digitizer. Once the digitizer receives the trigger and starts acquiring data, it sends out a trigger onto one of its output ports. This signal is sent to trigger a multi-channel delay generator, which then outputs TTL signals to start one or multiple cameras. Because of the insertion delay of both the delay generator and the cameras, a camera trigger delay has to be set on the delay generator to synchronize with the next pulse. This pulse shift can be corrected easily during data processing. On the software side, due to latency and indeterministic nature of the Windows operating system, a tight synchronization at the millisecond level cannot be achieved. Our solution is to initialize the camera first and set it on waiting for triggers. In this case, as long as the trigger from the digitizer chain arrives after the camera is ready, the synchronization between camera and digitizer can be achieved. This scheme has worked well and eliminated the need for costly real-time hardware and software systems. Other synchronization schemes are certainly possible: we had to employ another method utilizing the time stamps of a camera and a digitizer for synchronization when the laser repetition rate was quite high at 80 megahertz (MHz). In this case, neither the digitizer nor the camera can trigger that fast.

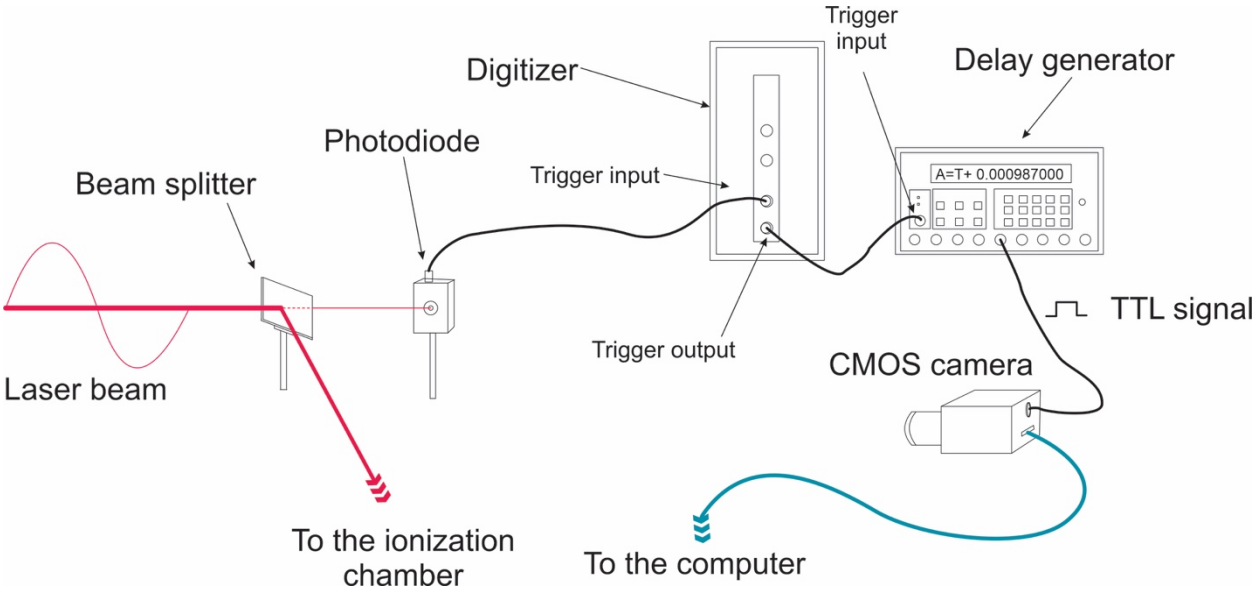

Fig. 5 A diagram illustrating the 3D VMI trigger and synchronization scheme.

4.5 System calibration

Once the (x, y, t) coordinates of each event have been measured, it is time to retrieve the 3D momentum vectors. With a uniform electric field such as that employed in a COLTRIMS spectrometer, this is straightforward and momentum vectors can be calculated with analytical equations, provided that the dimensions of the spectrometer are known accurately. With a VMI spectrometer, this situation is more complex depending on different designs. However, the linearity between hit positions on the detector (x,y) and velocity vectors (v_x and v_y) as well as that between time of flight (t) and velocity vector (v_z) are well maintained (Fig. 6). This makes the retrieval of p_x, p_y and p_z reasonably easy. The required slopes and intercepts of the two lines can be obtained using systems with known kinetic energies. In the Li lab, photoelectrons arising from strong field above threshold ionization (ATI) in noble gases are used to calibrate electron momentum retrieval. This is because neighboring ATI rings are separated by an energy spacing of one photon. For ions, dissociative double ionization of methyl iodide is often employed to achieve calibration. We should note, with the SIMION software, it is possible to reconstruct the spectrometer accurately enough to achieve direct transformation between (x,y,t) and (p_x, p_y, p_z).

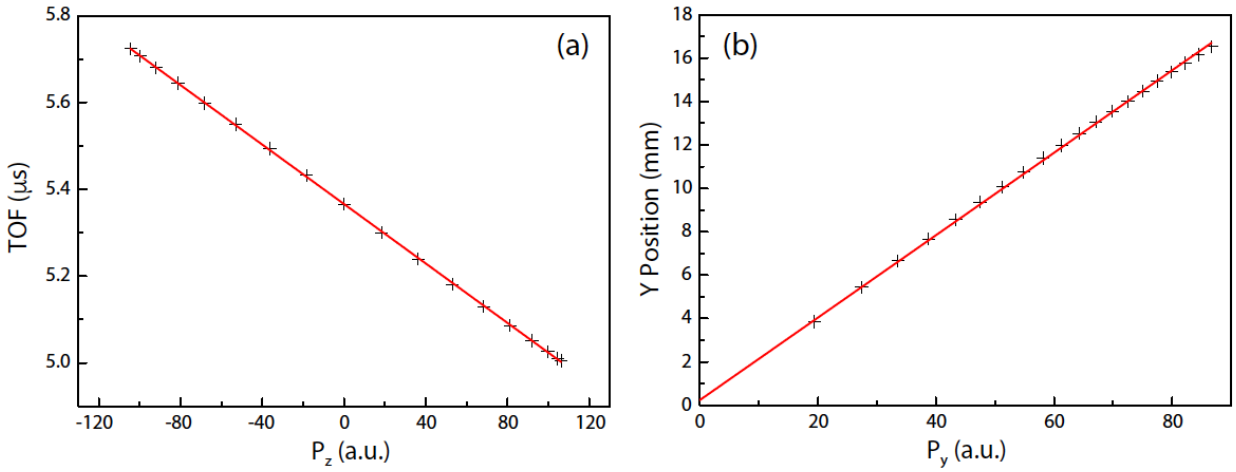

Fig. 6 In a typical VMI spectrometer, the linear relationship between: (a) TOF and p_z momentum; and (b) y position and p_y momentum are well preserved and this facilitates the conversion between (x, y, t) and (p_x p_y, p_z). The data were obtained from SIMION simulations using a slicing VMI setup and N_2^+ with kinetic energy up to 6 eV.

5. System performance characterization and method validation

The new 3D-VMI system and method were thoroughly validated and characterized. These include both single hit and multi-hit detection of both electrons and ions.

5.1 Single-hit performance

When only one event is captured on the camera frame and one peak is detected from the digitizer trace, the situation is relatively easy. However, due to the different detection efficiencies of the camera and the TOF systems (MCP or PMT), one system might fail in detecting the event (Fig. 7a). These events account for ~ 5% of the total counts after peak detection algorithm optimization. This is the first validation of the approach. The second validation is obtained from the correlation of digitizer peak amplitude and the camera spot intensity (Fig. 7b). These show that the position and time information are indeed from measuring the same event and that the employed cameras are indeed sensitive enough to capture the events.

After establishing the correlation between the digitizer and the camera the spatial and temporal resolution can be characterized. The spatial resolution of the system is determined by the camera pixel resolution and the lens magnification. The best native spatial resolution is 0.12 mm (with a camera resolution of 620x620 and an effective detector diameter of 75mm). The spatial resolution can be further improved by employing the center-of-mass centroiding algorithm and interpolation to achieve a sub-pixel resolution[76]. However, in most of the cases, other factors dominate the overall spatial resolution so that such an interpolation is not always needed.

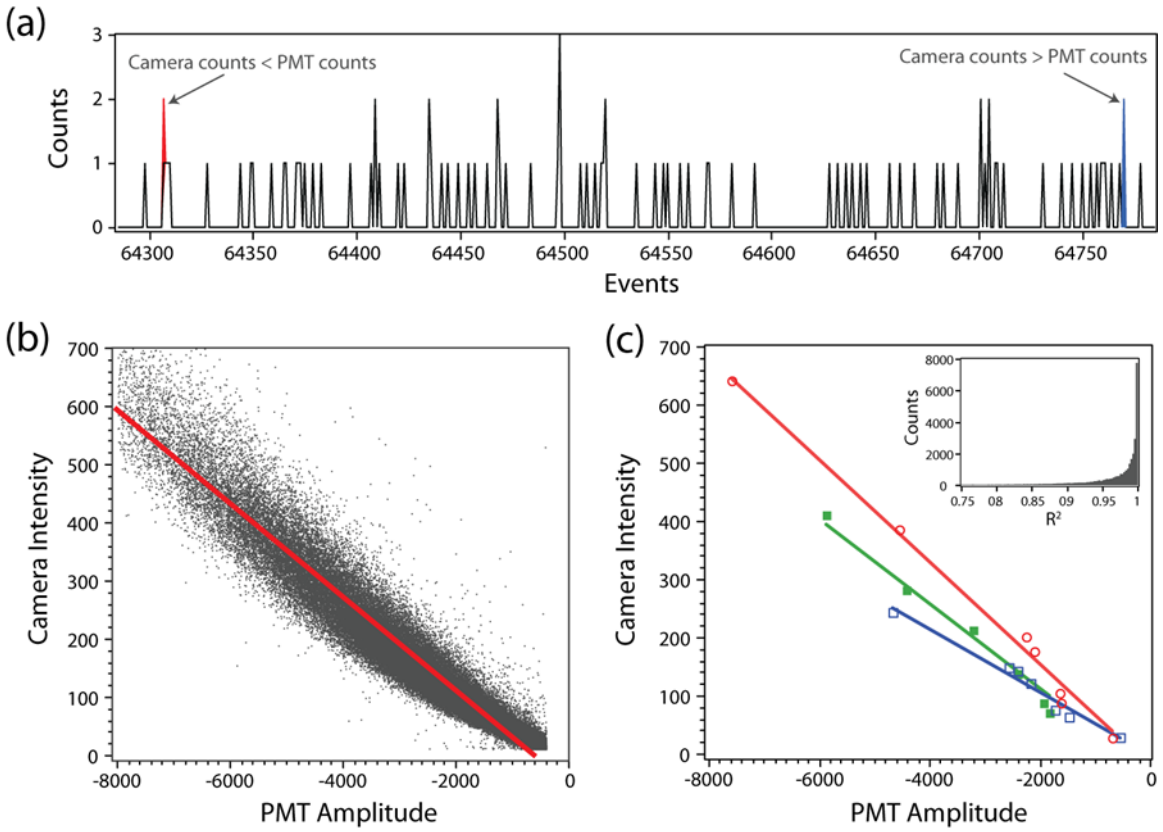

Fig. 7 (a) Ion counts registered by camera and PMT for each laser shot in data acquisition, two cases are shown where the ion counts are mismatched. These events are discarded. (b) The correlation between PMT peak amplitude and the ion spot intensity on camera. Linear fitting is shown by the red line. (c) The correlation between peak amplitude and camera intensity in three events with more than five ions. The inset shows a good R^2 distribution of linear fittings for all multi-hit (more than two) events within the same laser shot. (Reproduced from[15] with the permission from of AIP Publishing)

For ion imaging applications, a TOF resolution of one nanosecond is adequate and this can be easily achieved with the setup. However, the electron TOF spread is much smaller (often less than 10 ns), the P47+PMT scheme is not accurate enough to provide good temporal resolution. Instead, the timing signal from the grounded MCP front plate is picked off with a capacitive decoupling scheme. We achieved a good timing signal from the MCP with a rise time of 1.5 ns and a full width half maximum of 3 ns, enabling good TOF measurement accuracy. After aforementioned oversampling and trigger jitter suppression, we showed it is possible to achieve a TOF resolution of ~30 ps. The capabilities of the system were demonstrated in a study of above threshold ionization (ATI) of Xenon under strong field ionization conditions. Fig. 8 shows it is possible now to slice the electron Newton sphere with the achieved time resolution.

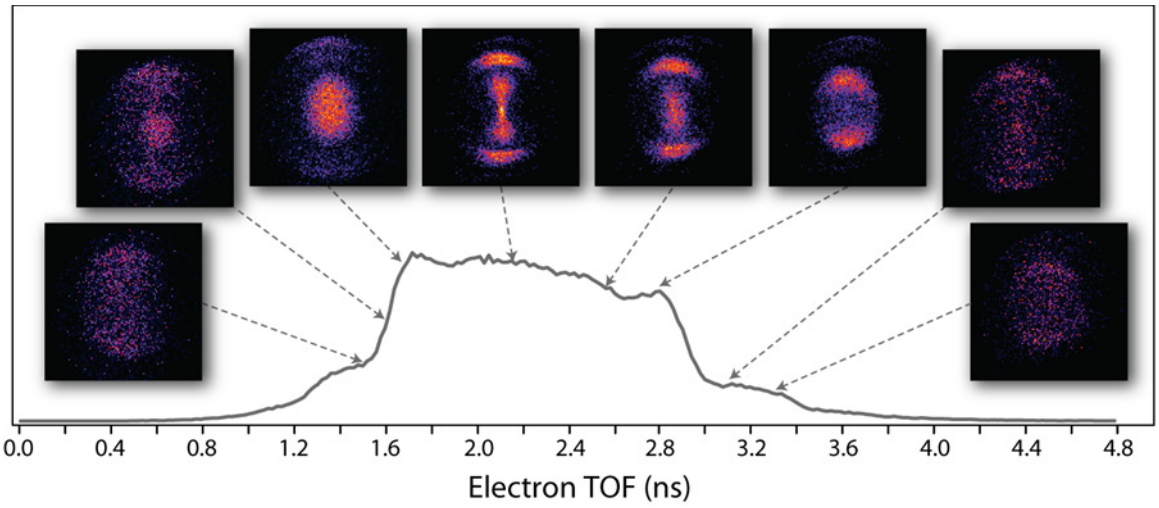

Fig. 8 Time slicing images at different electron time-of-flights – The temporal evolution of the electron (8 time slices of 32 ps) (Reproduced from [16] with the permission from of AIP Publishing)

As mentioned earlier the 3D imaging technique eliminates the need of image reconstruction methods and the necessity to have a cylindrically symmetrical electron Newton sphere. With this technique, we were able to measure complete 3D velocity distributions in a single measurement (Fig. 9).

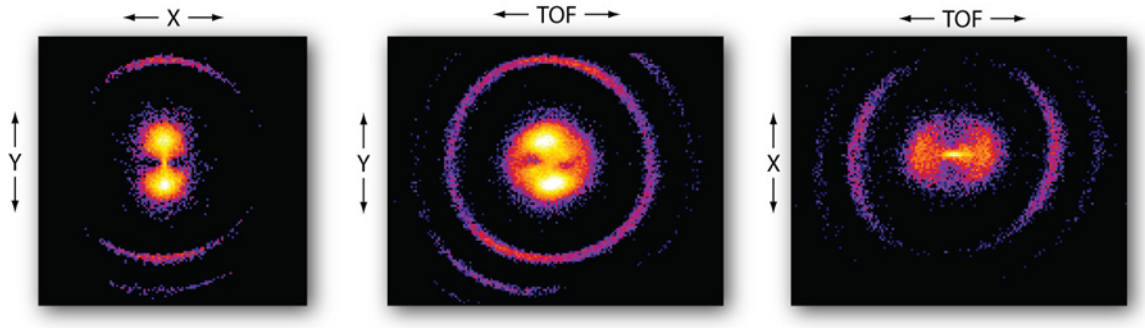

Fig. 9 Time and space slicing of the electron Newton Sphere from above threshold ionization of xenon. (Reproduced from[16] with the permission from of AIP Publishing)

5.2 Multi-hit performance

The capability of the system has been extended to achieve multi-hit detection. This capability is a direct result of the peak amplitude and the camera intensity correlation. The experimental observations showed a strong intensity correlation among tens of ions. The inset of Fig. 7c shows the R^2 distribution for three or more hits. Ion-ion coincidence 3D momentum imaging on strong field double ionization of methyl iodide was used showcase the multi-hit capability (Fig. 10). With the implementation of the intensity correlation algorithm and applying the momentum conservation constraint, 100% of the true coincidence events can be recovered.

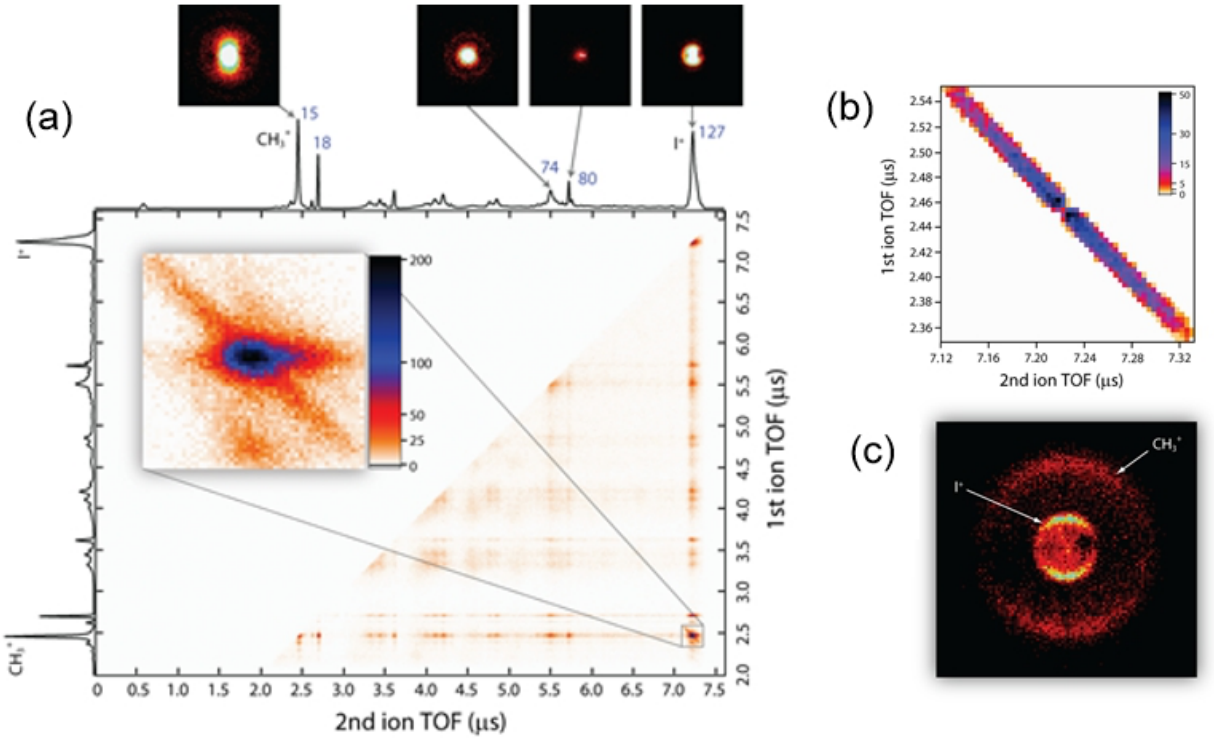

Fig. 10 (a) (Top) Ion momentum images of masses: 15: CH_3^+ and 127: I^+. (Bottom) 2D ion TOF spectrum of all two-hit events. The inset is the enlargement of 2D TOF around methyl cation and iodine cation. (b) Dissociative double ionization events of methyl iodide. (c) 2D velocity image of methyl cation and iodine cation resulting from dissociative double ionization. (Reproduced from[15] with the permission from of AIP Publishing)

With multi-hit electron detection, the system was further optimized to achieve an unprecedented deadtime reduction. As shown in Fig. 11, when two electrons come within a very short time separation the two pulses overlap or merge to form a single pulse. For such events, an advanced global fitting algorithm can be used. As the camera does not have a dead-time, it can capture two electrons within a short time provided that the electrons produce two spatially separated pixel clusters. If that situation is satisfied, the global fitting algorithm will be initiated to extract the time-of-flight information of the electrons from the waveform. The fitting procedure is as follows: (1) A standard single waveform is formed by averaging all the single hit waveforms. (2) Using the nonlinear Levenberg-Marquardt algorithm, the single hit waveform is fitted with a sum of two Gaussian functions to construct the basis function. (3) To obtain the positions and amplitudes from a registered double hit event from the camera, the waveform is fitted with a sum of the two basis functions. (4) Finally, by correlating the camera spot intensity with the amplitude the position and timing information for the two electron hits are obtained. In comparison to a simple peak detection algorithm, this timing analysis algorithm resulted a fourfold increase in two electron counts under normal experimental conditions. The shortest dead-time of 0.64 ns was observed by applying this algorithm. Another important feature of the detection system is the zero dead-time detection ability. This occurs in a situation where the camera captures a two-electron event, and the algorithm cannot successfully resolve them to single TOF events. In such cases a single TOF is assigned by

the fitting procedure. This results an uncertainty of ~ 0.7 ns in TOF while having accurate positional information.

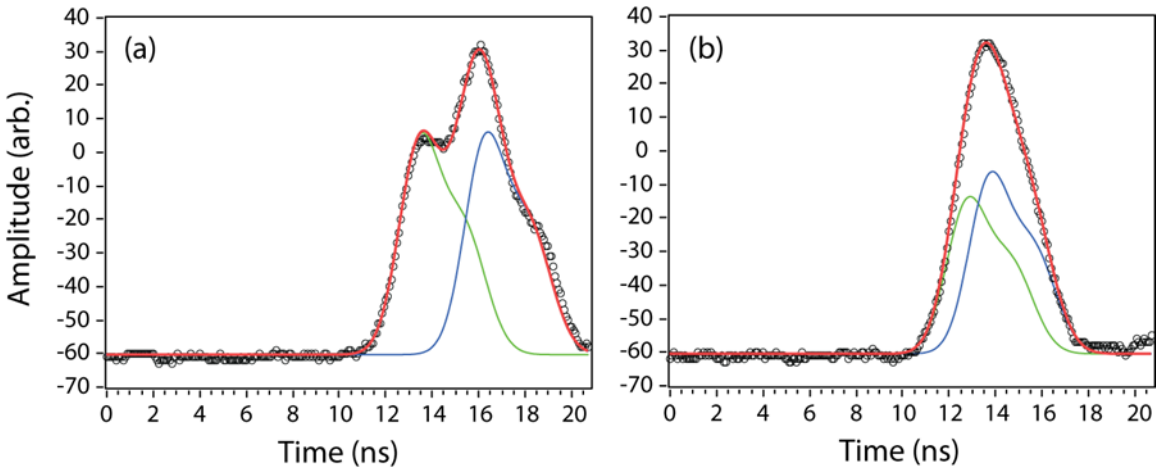

Fig. 11 (a) A pulse waveform from MCP showing two electrons arriving within 3 ns time interval (b) A pulse waveform from MCP showing two electrons arriving within 1 ns time interval. The fitted basis functions are shown in green and blue curves. (Reproduced from[17] with the permission from of AIP Publishing)

Further reduction of the deadtime was achieved recently by adopting a dye-based fast scintillator and a fast silicon photomultiplier (siPMT)[75] (Fig. 12). In this case, the siPMT provided ringing-free waveforms with a rise time of 1.2 ns and a FWHM of 2.7 ns. The timing analysis algorithm resulted the shortest resolvable time difference of 0.48 ns, the best deadtime achieved so far. A good correlation between the digitizer peak amplitude from Si-PM and the camera spot brightness facilitated the assignment of positional and temporal information for the detected electrons in a multi-hit event. The events on the diagonal line (Fig. 10a) represents the TOFs of two electron events that are not fully resolvable in TOF spectra due to an extremely short time difference between them (<0.48 ns). These events are not lost, and the same time-of-flight is assigned, achieving the zero-deadtime ability.

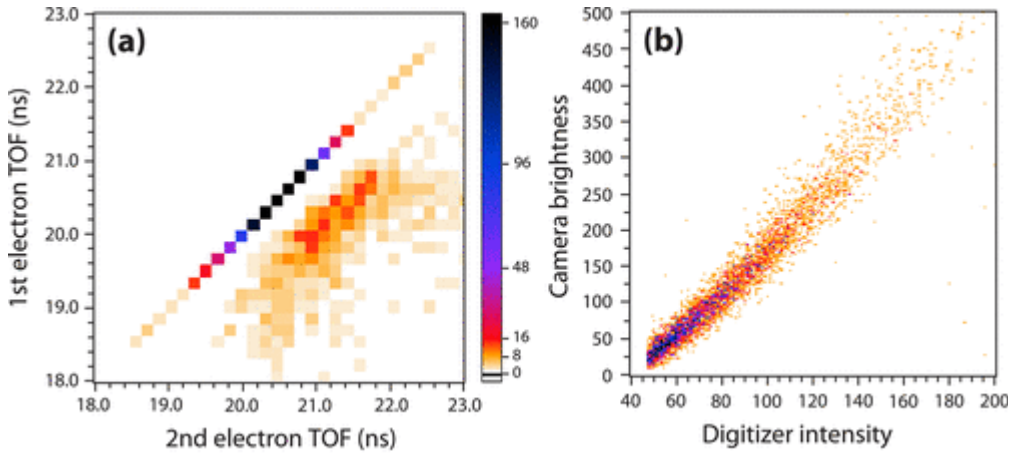

Fig. 12 The performance of two electron detection using the all-optical detection method (a) the 2D electron TOF showing the zero-deadtime detection (b) The correlation of camera spot intensity and the digitizer peak amplitude from the Si-PM for two electron events. (Adapted with permission from [75]. Copyright 2021 American Chemical Society.)

6. Specific instrumentation showcase

Based on the new 3D imaging system, the Li group has developed a variety of instrumentations to study chemical and surface dynamics in the past few years. These instrumentations demonstrate the versatile nature and high performance of the 3D imaging system. Here we showcase two of such implementations.

6.1 A single detector approach to ion-electron coincidence imaging

A typical photoelectron-photoion coincidence imaging apparatus can be considered as a double-sided VMI setup where the electrons and the ions are accelerated towards the detectors at the opposite ends[10, 77-79]. Compared to a conventional VMI setup, the added costs and complexities of such a design is the additional imaging detector and the electrostatic lenses. Since a conventional VMI setup is unidirectional, a way to implement both the ion and electron coincidence detection is through rapid switching of the electric field direction. This drives the electrons and ions towards the imaging detector at different time intervals due to the differences in their span of TOF and make the detection possible. This was first introduced by Lehmann and co-workers using a detector based on a DLD[80]. Zhao and co-workers further modified this design by replacing the DLD with a MCP/phosphor and a fast CMOS camera[81]. In their setup, only the 2D positional information of electrons was captured by a single camera by closing the shutter immediately after the electron arrival. Using a single camera to capture the positional information of ions and electrons and associating with the respective TOFs in such a situation is tricky as the same camera frame contains the flashes produced by both ions and electrons on the phosphor and could lead to mis-assignments. This was solved by adding an additional camera to the set-up[82].

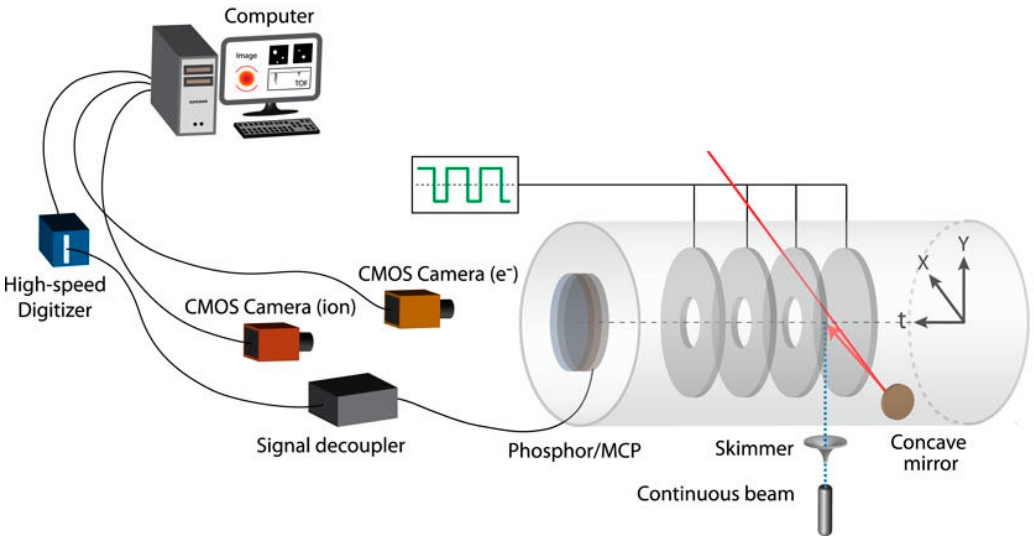

Fig. 13 The two camera VMI setup for ion and electron 3D coincidence momentum imaging. (Reproduced from[82] with the permission from of AIP Publishing)

In this setup, we adopted a special triggering scheme for the cameras exploiting the TOF differences between ions (> 1 μs) and electrons (< 100 ns) (Fig. 13). One camera is triggered to capture only the electron flashes on the screen by exposing the first 1 μs after the laser pulse and the other camera to expose after the first 1 μs to capture only the ions. As long as the camera trigger jitter is small (~1 μs), the scheme will work nicely. In this way, the mis-assignment of the positional and time information for the charged fragments can be avoided and the process becomes quite simple. Since ions and electrons are captured in separate camera frames, the multi-hit events of electrons or ions can also be resolved using the correlation between camera brightness and TOF peak heights. The 3D coincidence imaging capabilities of the new system were demonstrated in studying PENNA (2-phenylethyl-N, N-dimethylamine) dissociative double ionization.

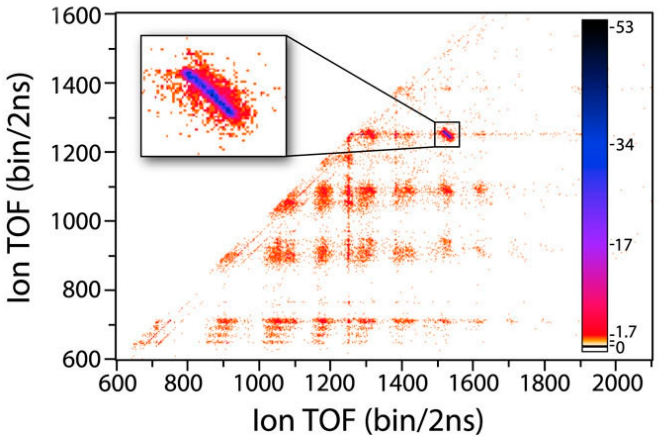

Fig. 14 The PIPICO map of the dissociative double ionization of PENNA the inset shows the dimethylamine monocation ($(N(CH_3)_2CH_2^+$), and benzyl monocation dissociation channel. (Reproduced from[82] with the permission from of AIP Publishing)

The photoion-photoion coincidence (PIPICO) map shows a dissociation channel producing dimethylamine monocation ($(N(CH_3)_2CH_2^+$), mass 58) and benzyl monocation (C_6H_5-CH_2^+, mass 91) (Fig. 14) while Fig. 15 shows the retrieved momentum distributions of both cations and coincident electrons, demonstrating the multi-hit 3D imaging capability of the single detector system.

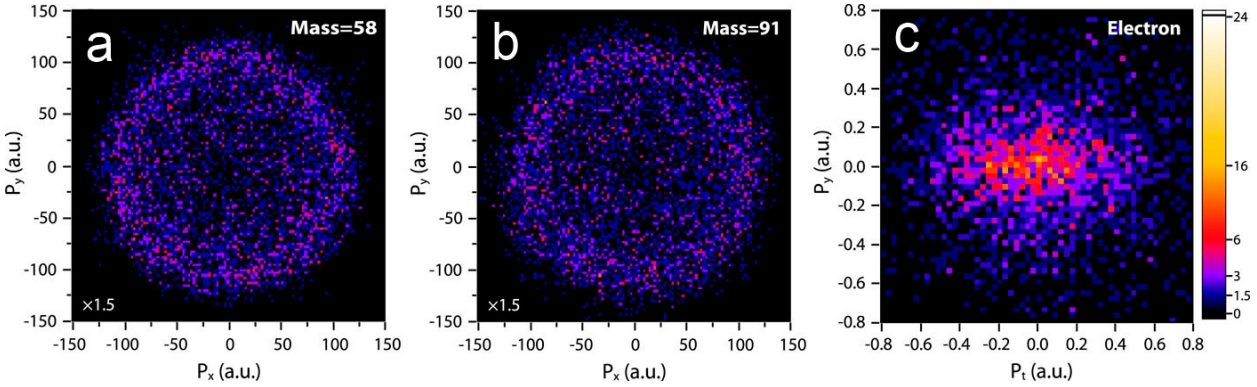

Fig. 15 XY momentum distributions of coincidence ion pairs of the (a) dimethylamine monocation ($N(CH_3)_2CH_2^+$ and (b) benzyl monocation ($C_6H_5–CH_2^+$ and (c) Yt momentum distribution of photoelectrons in coincidence with the ion pairs. (Reproduced from[82] with the permission from of AIP Publishing)

6.2 Towards one million hits per second with the camera-based 3D VMI system

One of the challenges in coincidence measurements is the false coincidence. To minimize this, the count rate has to be kept at a lower level. This, in turn results a long data acquisition times that are needed to achieve a data set with a reasonable statistics[83]. Therefore, coincidence experiment typically needs a system running at a high repetition rate. The camera-based 3D imaging system is capable of a few thousand events per second, which is sufficient to carry out a coincidence experiment. But it is far from being optimal. We note a delay-line detector is capable of acquiring 1 Mhits/s. We also note detector speed is not the only concern when performing coincidence measurements. A suitable laser system capable of MHz is usually the bigger hurdle than a detector. Nonetheless, is it possible to achieve 1 Mhits/s with the camera-based system, considering its superior multi-hit capability.

In an effort of achieving higher frame rates, the CMOS camera in the 3D momentum imaging system[84, 85] was replaced with a Tpx3Cam optical imager. This novel time stamping optical imager with the Timepix3 chip was a successor to the Timepix chip that was introduced in 2013. It has an improved time resolution of ~ 1.5 ns together with simultaneous measurement of time of arrival (TOA)/time above threshold (TOT) and reduced dead time of 0.5µs[86]. This was first used by Weinacht and co-workers in a coincidence velocity map imaging experiment[87]. One of the main advantages of the Tpx3Cam over the conventional cameras is the amount of data it generates. A conventional camera outputs a fixed number of pixels in a frame, even with zero-valued pixels. This is the reason for the huge amount of data at a high frame rate. The event-driven approach in Timepix3 sensor only captures the data of interest by recording the time when a certain predefined signal intensity is exceeded in an individual pixel, and this reduces the amount of data generated and supports a continuous readout up to 80 MHits/s[88, 89]. Our 3D imaging system can readily incorporate such a camera to replace the CMOS camera to achieve a much higher event rate (Fig. 16).

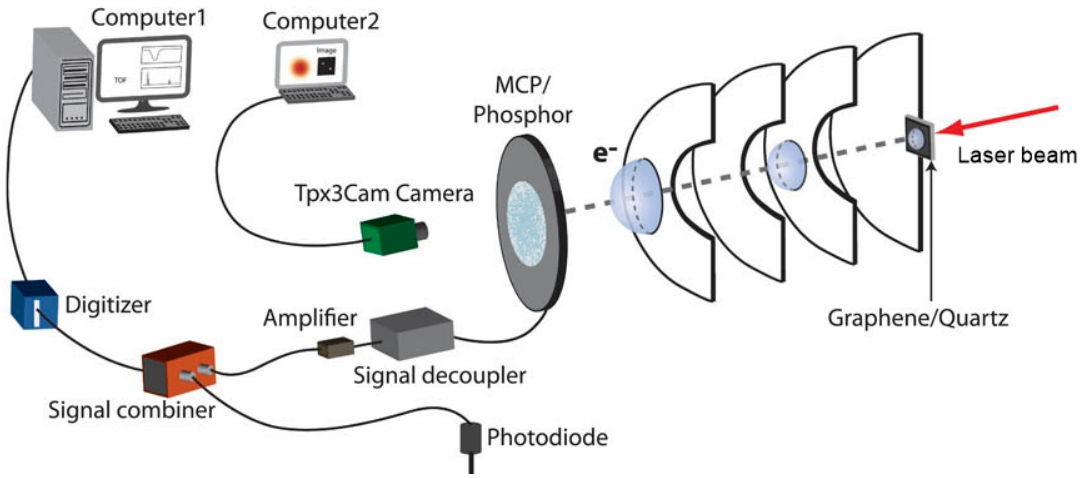

Fig. 16 The ultrafast 3D momentum imaging setup with a Tpx3Cam. (Reproduced from [74] with the permission from of AIP Publishing)

The capabilities of the new system were demonstrated using a high repetition laser system at a rate of 80 MHz to detect the photo-induced thermionic emission from graphene. The experimental scheme composed of a high-speed digitizer (AlazarTech ATS9373) which was employed to acquire the MCP signal for electron hits at a rate of up to one million waveforms per second and the Tpx3Cam camera operated to register the position coordinates of the events with time stamps. Because it is not possible to trigger the camera and the digitizer at such high rate, the timestamps of events from the camera and that from the digitizer were used to synchronize the spatial and temporal information of an event. The 3D electron Newton hemisphere constructed from the acquired 3D measurements were consistent with previous measurement and confirmed the observation of delayed electron emission at a lower event rate[90]. This shows that such a system is able to achieve accurate TOF measurements of$\sim$ 30 ps while achieving an event rate approaching 1 Mhits/s.

7. **Applications of electron-ion coincidence 3D VMI – disentangling strong-field multielectron dynamics with angular streaking**

In this final section, we will discuss one of the interesting studies performed using the novel 3D coincidence VMI system. One of the formidable challenges in spectroscopy is to resolve complex coupled electronic and nuclear dynamics in the presence of strong laser fields. Molecular frame photoelectron angular distributions (MFPAD)[91], offer a robust method of revealing the structures of the ionizing orbitals. Furthermore, being a highly sensitive probe for electron dynamics, direct measurements of MFPADs of double ionization is highly desirable for polyatomic molecules. MFPAD measurements can be obtained by employing the angular streaking technique[92-94] and have been demonstrated in laser-oriented molecules[95] and randomly oriented molecules[96]. When it comes to MFPAD measurements in correlated multielectron dynamics, there are technical difficulties (detection deadtime) limiting the coincidence detection of two electrons. As we have shown earlier, the hybrid 3D photoelectron-photoion coincidence apparatus can be used in such situations to detect two coincident electrons efficiently.

In this study we employed the 3D two-electron angular streaking (*3D-2eAS*) method implemented with the 3D ion-electron coincidence technique to measure the recoil-frame photoelectron angular distributions (RFPAD) of dissociative single- and double-ionization of methyl iodide. After acquiring the 3D momenta of electrons and ions in coincidence, the photoelectron angular distribution (PAD) was plotted. The recoil-frame electron momentum distribution shown in Fig. 16a was produced from the single ionization process of methyl iodide with respect to the fixed I^+ ion momentum direction in the plane of polarization.

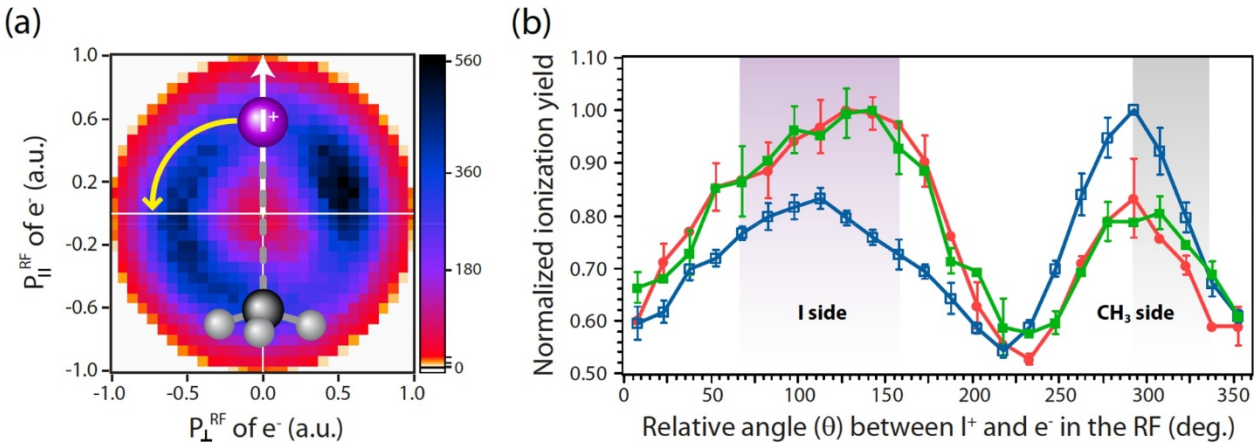

Fig. 17 (a) Recoil-frame electron momentum distribution obtained by coincidence measurements of electrons and I^+ for the dissociative single ionization of CH_3I. The I^+ recoil momentum is pointed up, indicated by the white arrow and the helicity of the circularly polarized light is shown by the yellow curved arrow. (b) RFPADs for dissociative single ionization (blue line with open square points) and dissociative double ionization measured with quadruple coincidence (green line with closed square points, e1 + e2 + fragment 1 + fragment 2) and double coincidence (red line with closed circle points, e + fragment), respectively. The angle θ is defined as the relative angle between the recoil direction of the iodine ion and the ejected electron (the angle increases anticlockwise). The gray and purple shaded areas correspond to the distributions of electrons escaping from the CH_3 and I sides, respectively. Note that the two curves were normalized to their own maxima. (Reprinted with permission from [97]. Copyright 2018 American Chemical Society.)

Since the helicity of the polarized light is known, the site of ionization (CH_3^+ or I^+) can be identified by implementing the angular streaking technique. As the instantaneous electric field vector potential is perpendicular to the electric field at the moment of ionization, the final momentum of the electrons that are released along the C-I bond will be rotated about 90 degrees away from the recoil ion momentum. The black narrow and broad island like features in the right and left sides of the Fig. 17a represent the electrons ejected from CH_3 and I sides, respectively. There is a slight deviation of the electron momentum from 90 degrees that results from the attractive forces between the ionic core and the ejected electron. Figure 17b shows the angular dependent ionization for the single ionization (blue line with open squares) obtained from the radial integration of the electron momentum distribution shown in Fig. 17a.

Angular dependent ionization yields as obtained from RFPAD reflects characteristics of different orbitals. This can be exploited to resolve contributions of different orbitals to the total ionization. For single ionization, TDCI-CAP calculations[98-100] were able to reproduce the experimental angular dependent ionization yield and showed the relative contribution from HOMO (a doubly degenerate π orbitals from the lone pair on the I atom) and that from HOMO-1 (σ type orbital responsible for C-I bond to be around 1:3 (Fig. 18).

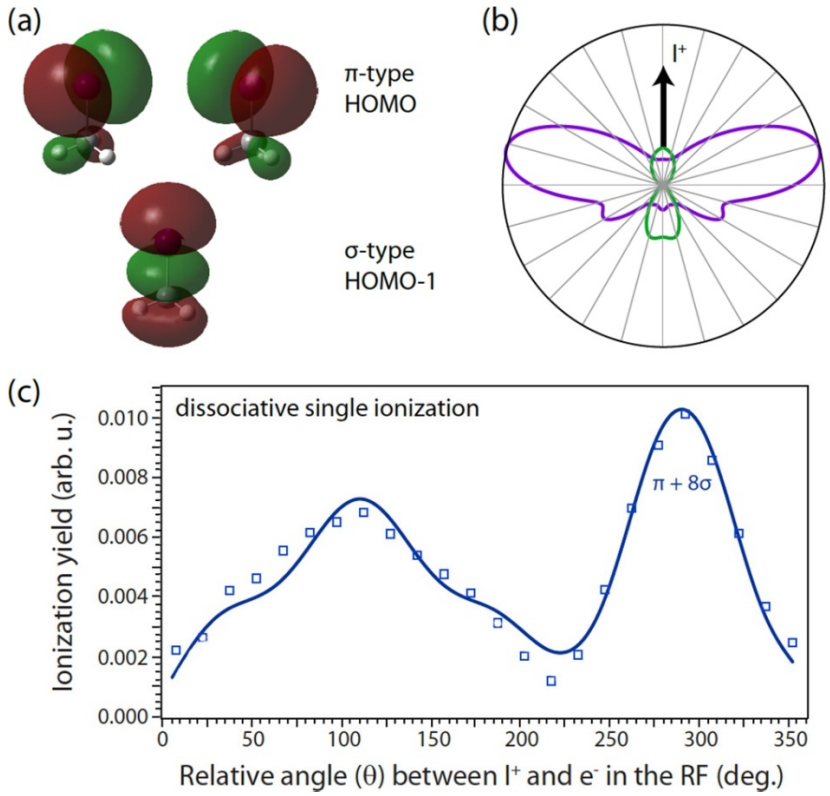

Fig. 18 (a) Electron density plots of the degenerate highest occupied molecular orbitals (HOMO) and HOMO-1 of CH_3I. (b) Contributions from different orbitals: π-type HOMO (purple), and σ-type HOMO-1 (green) to the calculated angular-dependent ionization yields for static electric fields of 0.055 au (1.06×10^{14} W/cm^2). The I^+ recoil direction indicates the C-I bond orientation. (c) Comparison between experimental (blue open squares) and calculated angular-dependent ionization yield, showing the contribution from HOMO and HOMO−1 orbitals. (Reprinted with permission from [97]. Copyright 2018 American Chemical Society.)

For double ionization events, when measuring the double coincidence events between one iodine ion and one electron with a specified total ion kinetic energy value of ~ 4.5 eV, the results (red line with closed circles in Fig. 17b) showed a good agreement with that of quadruple coincidence by detecting the two fragment ions (CH_3^+ and I^+) and two electrons (green line with closed squares in Fig. 17b). This is a validation of the efficient electron-electron coincidence measurements that can used for the correlated electron dynamics studies. There is a clear difference between the double ionization and the single ionization (Fig. 17b) as the electrons from the double ionization primarily comes from the I side. This suggests significant contribution from the Π orbital.

Theoretically, only sequential double ionization is considered as the recollision is suppressed under circular polarization. The angular dependent ionization yields were calculated for the lowest energy pathways for producing dications involving the ionization of HOMO(||), HOMO(⊥), and HOMO-1 in neutral molecule followed by a second ionization of corresponding cations, namely Π_1, Π_2, and Σ cations, respectively. The HOMO(||) and HOMO(⊥) orbitals are the two degenerate orbitals lying parallel and perpendicular to the plane of polarization (Fig. 18a).

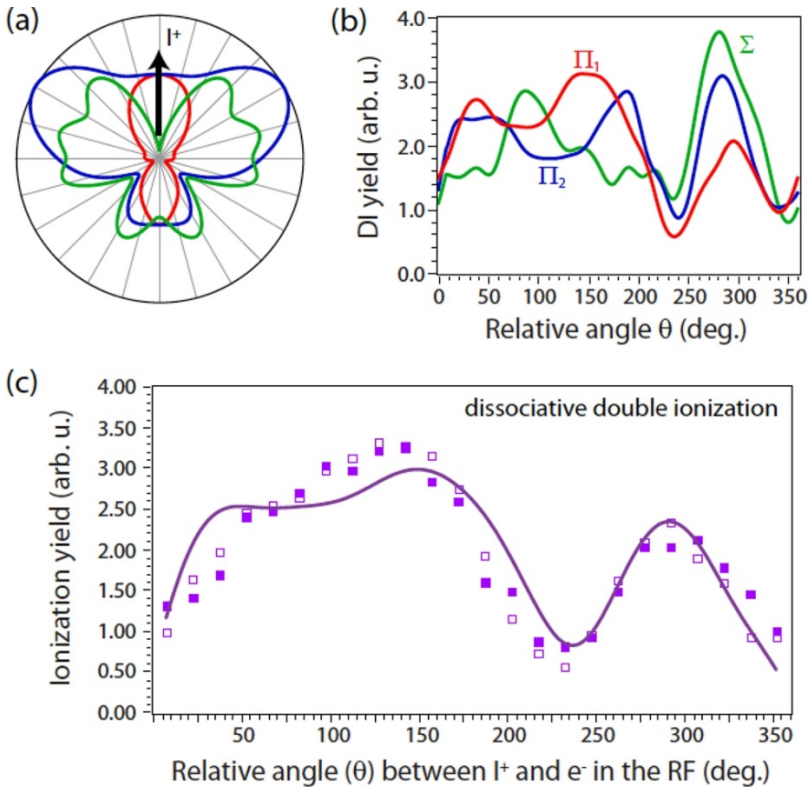

Fig. 19 (a) Calculated angular-dependent ionization yields for Π_1(red), Π_2 (blue), and Σ (green) cations at a field strength of 0.065 au (1.48×10^{14} W/cm^2). (b) The angular-dependent double ionization yield for three different pathways with Π_1(red), Π_2 (blue) and Σ (green) cations as the intermediate states. (c) Comparison between experimental (solid square from quadruple coincidence measurement, empty square from double coincidence measurement) and calculated angular-dependent ionization yield (purple line) for dissociative double ionization. (Reprinted with permission from [97]. Copyright 2018 American Chemical Society.)

From the theoretical investigation, it is possible to find out the orbital contributions for the angular dependent ionization yields. Three ionization processes were considered, (1) HOMO(||) → Π_1 cation → dication ($\sigma^1\pi_1^1\pi_2^2$), (2) HOMO(⊥) → Π_2 cation → dication ($\sigma^2\pi_1^1\pi_2^1$) and (3) HOMO−1 → Σ cation→ dication ($\sigma^1\pi_1^1\pi_2^2$). The results from the calculations (Fig. 19b) show a significantly different angular dependent ionizations yields for the first and third process despite having the similar electron configuration in the final dication: both losing one electron each from HOMO and HOMO-1 orbitals. This suggests the significance of orbital relaxation and reorganization that occur between the first and second ionization, and the order of losing electrons in the process. The theoretical angular dependent ionization obtained by a weighted sum of three dissociation pathways with a ratio of 0.68:0.20:0.11, shows a good agreement with the experimental result (Fig. 19c).

With the high electron-electron coincidence detection capability of the imaging system, the multielectron dynamics involved in the dissociative double ionization process can be studied. For this, a 2D photoionization spectrum can be constructed (Fig. 20a). This is plotted with the angular dependent ionization yields of the first and the second electrons.

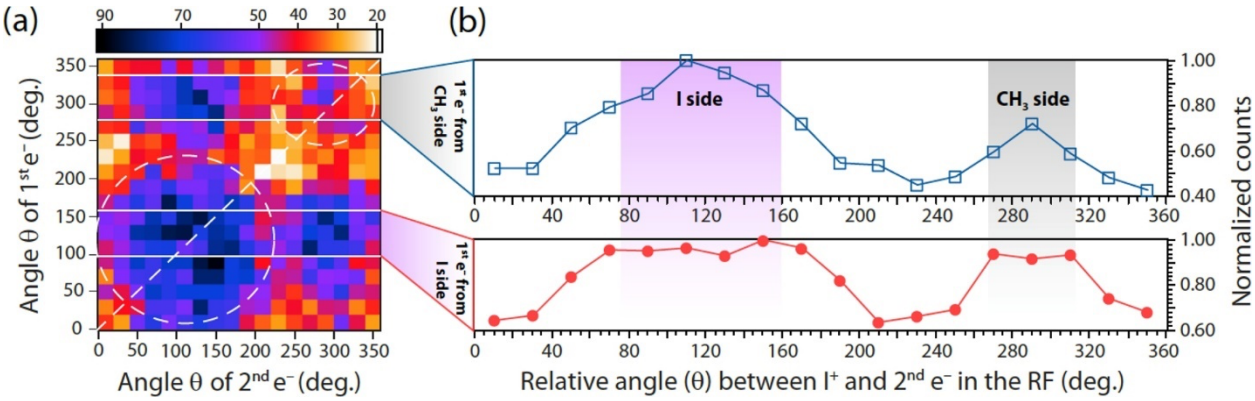

Fig. 20 (a) 2D photoionization spectrum showing the 2D electron–electron angular correlation in the recoil frame of the dissociative double ionization of CH_3I. The angle θ is defined as the relative angle between the recoil direction of the iodine ion (θ = 0°) and the ejected electron. The white dashed ovals indicate the two diagonal peaks. (b) Angular-dependent ionization yields of the second electron in the recoil frame. The top panel corresponds to the case when the first electron is released from the CH_3 side, and the bottom panel corresponds to the case when the first electron is released from the peak in the I side. (Reprinted with permission from [97]. Copyright 2018 American Chemical Society.)

The diagonal peaks in the plot represent the instance of ionization of both electrons from the same site and the off-diagonal peaks represent the sequential ionization from two different sites. Even though there are two diagonal peaks (Fig. 20a), the intensities are quite different. The weakest diagonal peak at (290°, 290°) suggests double ionization from CH_3 site is not favored. This can be understood by taking the ionizing orbitals on the CH_3 site into account. These are the low-lying orbitals, HOMO-1 and HOMO-2 which ionize to produce highly excited dications, therefore have a lower ionization probability. In contrast the ionization is highly favored on the I site showing the strongest diagonal feature at (120°, 120°). Figure 20b shows an enhancement of second ionization on CH_3 site if the first ionization occurs on the I site. Theoretical calculations reveal that this preference of ionization is not the result of ionizing the same HOMO orbital to produce the dication. Instead the ionization follows the dominant ionization channel HOMO(||) → Π_1 cation → dication ($\sigma^1\pi_1^1\pi_2^2$) where both of the ionization steps dominated by ionizing the electron on I site.

The example clearly showcased the power of highly differential measurements such as quadruple coincidence achieved with 3D-VMI. Together with theory, it can provide unprecedented details on complex ionization/dissociation dynamics in polyatomics. The same technique (*3D-2eAS*) was also used to resolve attosecond electron correlation dynamics in large molecules such as benzene[101].

Conclusion and Outlook

The 3D momentum imaging system demonstrated in this tutorial utilizes affordable state-of-the-art CMOS technology, delicate synchronization schemes and advanced acquisition and analysis algorithms to achieve unprecedented performance. The system is highly versatile and extremely re-configurable, as shown by many different instrumentations employing the imaging system. Even though the technique was born out of a conventional 2D-VMI setup, its full 3D imaging capability and fast acquisition speed allows the system to be used in many applications such as coincidence imaging, slice imaging[16] and angular resolved photoemission spectroscopy (ARPES)[90]. The unique capability of a zero deadtime

detection of electrons has made direct measurement of electron momentum correlation possible[101, 102]. This is particularly exciting for attosecond science because electron dynamics/correlation is one of its main foci. However, even in a conventional VMI setup, adding 3D capability to the system costs minimum effort but gains huge performance and capability boost[103]. To facilitate the adoption of 3D-VMI in broader scientific communities, we are preparing to release a free version of the image acquisition/analysis program package to the community in the near future.

Acknowledgement

Research supported by the U.S. Department of Energy (DOE), Office of Science, Basic Energy Sciences (BES), under Award # DE-SC0020994 and National Science Foundation (NSF), AMO-E program, under Award #2012098. We wish to thank Prof. Arthur Suits for helpful comments.

References

[1] Diesen R W, Wahr J C and Adler S E 1969 Photochemical Recoil Spectroscopy *J. Chem. Phys.* **50** 3635-6

[2] Riley S J and Wilson K R 1972 Excited Fragments from Excited Molecules - Energy Partitioning in Photodissociation of Alkyl Iodides *Faraday Discussions* **53** 132-46

[3] Busch G E, Mahoney R T, Morse R I and Wilson K R 1969 Translational Spectroscopy: Cl2 Photodissociation *J. Chem. Phys.* **51** 449-50

[4] Lee Y T, McDonald J D, LeBreton P R and Herschbach D R 1969 Molecular Beam Reactive Scattering Apparatus with Electron Bombardment Detector *Rev. Sci. Instrum.* **40** 1402-8

[5] Vasudev R, Zare R N and Dixon R N 1983 Dynamics of Photo-Dissociation of Hono at 369-Nm - Motional Anisotropy and Internal State Distribution of the Oh Fragment *Chem. Phys. Lett.* **96** 399-402

[6] Vasudev R, Zare R N and Dixon R N 1984 State-Selected Photodissociation Dynamics - Complete Characterization of the Oh Fragment Ejected by the Hono a-Approximately State *J. Chem. Phys.* **80** 4863-78

[7] Murphy E J, Brophy J H, Arnold G S, Dimpfl W L and Kinsey J L 1979 Velocity and Angular-Distributions of Reactive Collisions from Fourier-Transform Doppler Spectroscopy - 1st Experimental Results *J. Chem. Phys.* **70** 5910-1

[8] Chandler D W and Houston P L 1987 Two-dimensional imaging of state-selected photodissociation products detected by multiphoton ionization *J. Chem. Phys.* **87** 1445-7

[9] Eppink A and Parker D 1997 Velocity Map Imaging of Ions and Electrons Using Electrostatic Lenses: Application in Photoelectron and Photofragment Ion Imaging of Molecular Oxygen *Rev. Sci. Instrum.* **68** 3477

[10] Ullrich J, Moshammer R, Dorn A, Dorner R, Schmidt L P H and Schniidt-Bocking H 2003 Recoil-ion and Electron Momentum Spectroscopy: Reaction Microscopes *Rep. Prog. Phys.* **66** 1463-545

[11] Gebhardt C R, Rakitzis T P, Samartzis P C, Ladopoulos V and Kitsopoulos T N 2001 Slice imaging: A new approach to ion imaging and velocity mapping *Rev. Sci. Instrum.* **72** 3848-53

[12] Townsend D, Minitti M and Suits A 2003 Direct Current Slice Imaging *Rev. Sci. Instrum.* **74** 2530

[13] Lin J J, Zhou J, Shiu W and Liu K 2003 Application of time-sliced ion velocity imaging to crossed molecular beam experiments *Rev. Sci. Instrum.* **74** 2495-500

[14] Takahashi M, Cave J P and Eland J H D 2000 Velocity imaging photoionization coincidence apparatus for the study of angular correlations between electrons and fragment ions *Rev. Sci. Instrum.* **71** 1337-44

[15] Lee S K, Cudry F, Lin Y F, Lingenfelter S, Winney A H, Fan L and Li W 2014 Coincidence ion imaging with a fast frame camera *Rev. Sci. Instrum.* **85** 123303
[16] Lee S K, Lin Y F, Lingenfelter S, Fan L, Winney A H and Li W 2014 Communication: Time- and space-sliced velocity map electron imaging *J. Chem. Phys.* **141** 221101
[17] Lin Y F, Lee S K, Adhikari P, Herath T, Lingenfelter S, Winney A H and Li W 2015 Note: An improved 3D imaging system for electron-electron coincidence measurements *Rev. Sci. Instrum.* **86** 096110
[18] Shepp L A and Logan B F 1974 Fourier Reconstruction of a Head Section *Ieee T Nucl Sci* **Ns21** 21-43
[19] Strickland R N and Chandler D W 1991 Reconstruction of an Axisymmetrical Image from Its Blurred and Noisy Projection *Appl Optics* **30** 1811-9
[20] Vrakking M J J 2001 An iterative procedure for the inversion of two-dimensional ion/photoelectron imaging experiments *Rev. Sci. Instrum.* **72** 4084-9
[21] Manzhos S and Loock H P 2003 Photofragment image analysis using the Onion-Peeling Algorithm *Comput. Phys. Commun.* **154** 76-87
[22] Dribinski V, Ossadtchi A, Mandelshtam V A and Reisler H 2002 Reconstruction of Abel-transformable images: The Gaussian basis-set expansion Abel transform method *Rev. Sci. Instrum.* **73** 2642
[23] Eppink A T J B, Wu S-m and Whitaker B J 2003 *Imaging in Molecular Dynamics: Technology and Applications,* ed B J Whitaker (Cambridge: Cambridge University Press) pp 65-112
[24] Garcia G A, Nahon L and Powis I 2004 Two-dimensional charged particle image inversion using a polar basis function expansion *Rev. Sci. Instrum.* **75** 4989-96
[25] Renth F, Riedel J and Temps F 2006 Inversion of velocity map ion images using iterative regularization and cross validation *Rev. Sci. Instrum.* **77** 033103
[26] Dick B 2014 Inverting ion images without Abel inversion: maximum entropy reconstruction of velocity maps *Phys. Chem. Chem. Phys.* **16** 570-80
[27] Gerber T, Liu Y, Knopp G, Hemberger P, Bodi A, Radi P and Sych Y 2013 Charged particle velocity map image reconstruction with one-dimensional projections of spherical functions *Rev. Sci. Instrum.* **84** 033101
[28] Bass M J, Brouard M, Clark A P and Vallance C 2002 Fourier moment analysis of velocity-map ion images *J. Chem. Phys.* **117** 8723-35
[29] Ashfold M N R, Nahler N H, Orr-Ewing A J, Vieuxmaire O P J, Toomes R L, Kitsopoulos T N, Garcia I A, Chestakov D A, Wu S M and Parker D H 2006 Imaging the dynamics of gas phase reactions *Phys. Chem. Chem. Phys.* **8** 26-53
[30] Chestakov D A, Wu S M, Wu G R, Parker D H, Eppink A T J B and Kitsopoulos T N 2004 Slicing using a conventional velocity map imaging setup: O-2, I-2, and I-2(+) photodissociation *J. Phys. Chem. A* **108** 8100-5
[31] Ryazanov M and Reisler H 2013 Improved sliced velocity map imaging apparatus optimized for H photofragments *J. Chem. Phys.* **138** 144201
[32] Moradmand A, Slaughter D S, Landers A L and Fogle M 2013 Dissociative-electron-attachment dynamics near the 8-eV Feshbach resonance of CO2 *Phys. Rev. A* **88** 022711
[33] Thompson J O F, Amarasinghe C, Foley C D, Rombes N, Gao Z, Vogels S N, van de Meerakker S Y T and Suits A G 2017 Finite slice analysis (FINA) of sliced and velocity mapped images on a Cartesian grid *J. Chem. Phys.* **147** 074201
[34] Thompson J O F, Amarasinghe C, Foley C D and Suits A G 2017 Finite slice analysis (FINA)—A general reconstruction method for velocity mapped and time-sliced ion imaging *J. Chem. Phys.* **147** 013913

[35] Kauczok S, Gödecke N, Chichinin A I, Veckenstedt M, Maul C and Gericke K H 2009 Three-dimensional velocity map imaging: Setup and resolution improvement compared to three-dimensional ion imaging *Rev. Sci. Instrum.* **80** 083301
[36] Chichinin A I, Einfeld T, Maul C and Gericke K H 2002 Three-dimensional imaging technique for direct observation of the complete velocity distribution of state-selected photodissociation products *Rev. Sci. Instrum.* **73** 1856-65
[37] Dinu L, Eppink A T J B, Rosca-Pruna F, Offerhaus H L, van der Zande W J and Vrakking M J J 2002 Application of a time-resolved event counting technique in velocity map imaging *Rev. Sci. Instrum.* **73** 4206-13
[38] Koszinowski K, Goldberg N T, Pomerantz A E and Zare R N 2006 Construction and calibration of an instrument for three-dimensional ion imaging *J. Chem. Phys.* **125** 133503
[39] Hanold K A, Luong A K, Clements T G and Continetti R E 1999 Photoelectron–multiple-photofragment coincidence spectrometer *Rev. Sci. Instrum.* **70** 2268-76
[40] Suits A G 2018 Invited Review Article: Photofragment imaging *Rev. Sci. Instrum.* **89** 111101
[41] Chichinin A I, Gericke K H, Kauczok S and Maul C 2009 Imaging chemical reactions – 3D velocity mapping *Intl. Rev. Phys. Chem.* **28** 607-80
[42] Ballabriga R, Campbell M and Llopart X 2018 Asic developments for radiation imaging applications: The medipix and timepix family *Nucl Instrum Meth A* **878** 10-23
[43] Vallerga J, McPhate J, Mikulec B, Tremsin A, Clark A and Siegmund O 2004 Noiseless imaging detector for adaptive optics with kHz frame rates *Advancements in Adaptive Optics, Pts 1-3* **5490** 1256-67
[44] Vallerga J, McPhate J, Tremsin A and Siegmund O 2009 The current and future capabilities of MCP based UV detectors *Astrophys Space Sci* **320** 247-50
[45] Gademann G, Huismans Y, Gijsbertsen A, Jungmann J, Visschers J and Vrakking M J J 2009 Velocity map imaging using an in-vacuum pixel detector *Rev. Sci. Instrum.* **80** 103105
[46] Wiza J L 1979 Microchannel Plate Detectors *Nucl Instrum Methods* **162** 587-601
[47] Lapington J S 2004 A comparison of readout techniques for high-resolution imaging with microchannel plate detectors *Nucl Instrum Meth A* **525** 361-5
[48] Martin C, Jelinsky P, Lampton M, Malina R F and Anger H O 1981 Wedge-and-Strip Anodes for Centroid-Finding Position-Sensitive Photon and Particle Detectors *Rev. Sci. Instrum.* **52** 1067-74
[49] Siegmund O H W, Lampton M, Bixler J, Chakrabarti S, Vallerga J, Bowyer S and Malina R F 1986 Wedge and Strip Image Readout Systems for Photon-Counting Detectors in Space Astronomy *J Opt Soc Am A* **3** 2139-45
[50] Jagutzki O, Lapington J S, Worth L B C, Spillman U, Mergel V and Schmidt-Böcking H 2002 Position sensitive anodes for MCP read-out using induced charge measurement *Nucl. Instr. Meth. Phys. Res. A* **477** 256-61
[51] Saito N, Heiser F, Hemmers O, Wieliczek K, Viefhaus J and Becker U 1996 Kinetic-energy- and angular-resolved fragmentation of CO in vibrational-resolved C 1s excitation *Phys. Rev. A* **54** 2004-10
[52] Becker J, Beckord K, Werner U and Lutz H O 1994 A system for correlated fragment detection in dissociation experiments *Nucl. Instr. Meth. Phys. Res. A* **337** 409-15
[53] Eland J H D and Pearson A H 1990 Simple Radial Position-Sensitive Detector with Short Deadtime for Time-of-Flight and Coincidence Experiments *Meas Sci Technol* **1** 36-40
[54] Eland J H D 1994 Simple two-dimensional position sensitive detector with short dead-time for coincidence experiments *Meas Sci Technol* **5** 1501-4
[55] Ali I, Dorner R, Jagutzki O, Nuttgens S, Mergel V, Spielberger L, Khayyat K, Vogt T, Brauning H, Ullmann K, Moshammer R, Ullrich J, Hagmann S, Groeneveld K O, Cocke C L and Schmidt-Bocking

H 1999 Multi-hit detector system for complete momentum balance in spectroscopy in molecular fragmentation processes *Nucl Instrum Meth B* **149** 490-500
[56] Jagutzki O, Mergel V, Ullmann-Pfleger K, Spielberger L, Spillmann U, Dorner R and Schmidt-Bocking H 2002 A broad-application microchannel-plate detector system for advanced particle or photon detection tasks: large area imaging, precise multi-hit timing information and high detection rate *Nucl Instrum Meth A* **477** 244-9
[57] Lampton M, Siegmund O and Raffanti R 1987 Delay line anodes for microchannel-plate spectrometers *Rev. Sci. Instrum.* **58** 2298-305
[58] Amitay Z and Zajfman D 1997 A new type of multiparticle three-dimensional imaging detector with subnanosecond time resolution *Rev. Sci. Instrum.* **68** 1387-92
[59] Da Costa G, Vurpillot F, Bostel A, Bouet M and Deconihout B 2005 Design of a delay-line position-sensitive detector with improved performance *Rev. Sci. Instrum.* **76** 013304
[60] Wallauer R, Voss S, Foucar L, Bauer T, Schneider D, Titze J, Ulrich B, Kreidi K, Neumann N, Havermeier T, Schöffler M, Jahnke T, Czasch A, Schmidt L, Kanigel A, Campuzano J C, Jeschke H, Valenti R, Müller A, Berner G, Sing M, Claessen R, Schmidt-Böcking H and Dörner R 2012 Momentum spectrometer for electron-electron coincidence studies on superconductors *Rev. Sci. Instrum.* **83** 103905
[61] Jagutzki O, Cerezo A, Czasch A, Dorner R, Hattass M, Huang M, Mergel V, Spillmann U, Ullmann-Pfleger K, Weber T, Schmidt-Bocking H and Smith G D W 2002 Multiple hit readout of a microchannel plate detector with a three-layer delay-line anode *Ieee T Nucl Sci* **49** 2477-83
[62] Chandler D W, Thoman J W, Janssen M H M and Parker D H 1989 Photofragment Imaging - the 266-Nm Photodissociation of Ch3i *Chem. Phys. Lett.* **156** 151-8
[63] Hoops A A, Gascooke J R, Faulhaber A E, Kautzman K E and Neumark D M 2003 Fast beam studies of I2− and I2−·Ar photodissociation *Chem. Phys. Lett.* **374** 235-42
[64] Szpunar D E, Kautzman K E, Faulhaber A E and Neumark D M 2006 Photofragment coincidence imaging of small I−(H2O)n clusters excited to the charge-transfer-to-solvent state *J. Chem. Phys.* **124** 054318
[65] Strasser D, Urbain X, Pedersen H B, Altstein N, Heber O, Wester R, Bhushan K G and Zajfman D 2000 An innovative approach to multiparticle three-dimensional imaging *Rev. Sci. Instrum.* **71** 3092-8
[66] Deconihout B, Vurpillot F, Gault B, Da Costa G, Bouet M, Bostel A, Blavette D, Hideur A, Marte G and Brunel M 2007 Toward a laser assisted wide-angle tomographic atom-probe *Surf Interface Anal* **39** 278-82
[67] Ismail I M, Barat M, Brenot J-C, Fayeton J A, Lepère V and Picard Y J 2005 A zero dead-time, multihit, time and position sensitive detector based on micro-channel plates *Rev. Sci. Instrum.* **76** 043304
[68] Llopart X, Ballabriga R, Campbell M, Tlustos L and Wong W 2007 Timepix, a 65k programmable pixel readout chip for arrival time, energy and/or photon counting measurements *Nucl Instrum Meth A* **581** 485-94
[69] Nomerotski A, Brouard M, Campbell E, Clark A, Crooks J, Fopma J, John J J, Johnsen A J, Slater C, Turchetta R, Vallance C, Wilman E and Yuen W H 2010 Pixel Imaging Mass Spectrometry with fast and intelligent Pixel detectors *J. Instrum.* **5** C07007-C
[70] Vallance C, Brouard M, Lauer A, Slater C S, Halford E, Winter B, King S J, Lee J W L, Pooley D E, Sedgwick I, Turchetta R, Nomerotski A, John J J and Hill L 2014 Fast sensors for time-of-flight imaging applications *Phys. Chem. Chem. Phys.* **16** 383-95
[71] Urbain X, Bech D, Van Roy J-P, Géléoc M, Weber S J, Huetz A and Picard Y J 2015 A zero dead-time multi-particle time and position sensitive detector based on correlation between brightness and amplitude *Rev. Sci. Instrum.* **86** 023305

[72] Horio T and Suzuki T 2009 Multihit two-dimensional charged-particle imaging system with real-time image processing at 1000 frames/s *Rev. Sci. Instrum.* **80** 013706
[73] Fan L, Lee S K, Tu Y-J, Mignolet B, Couch D, Dorney K, Nguyen Q, Wooldridge L, Murnane M, Remacle F, Schlegel H B and Li W 2017 A new electron-ion coincidence 3D momentum-imaging method and its application in probing strong field dynamics of 2-phenylethyl-N, N-dimethylamine *J. Chem. Phys.* **147** 013920
[74] Debrah D A, Stewart G A, Basnayake G, Nomerotski A, Svihra P, Lee S K and Li W 2020 Developing a camera-based 3D momentum imaging system capable of 1 Mhits/s *Rev. Sci. Instrum.* **91** 023316
[75] Orunesajo E, Basnayake G, Ranathunga Y, Stewart G, Heathcote D, Vallance C, Lee S K and Li W 2021 All-Optical Three-Dimensional Electron Momentum Imaging *J. Phys. Chem. A* **125** 5220-5
[76] Li W, Chambreau S D, Lahankar S A and Suits A G 2005 Megapixel Ion Imaging with Standard Video *Rev. Sci. Instrum.* **76** 063106
[77] Tang X, Zhou X, Niu M, Liu S, Sun J, Shan X, Liu F and Sheng L 2009 A threshold photoelectron-photoion coincidence spectrometer with double velocity imaging using synchrotron radiation *Rev. Sci. Instrum.* **80** 113101
[78] Ablikim U, Bomme C, Osipov T, Xiong H, Obaid R, Bilodeau R C, Kling N G, Dumitriu I, Augustin S, Pathak S, Schnorr K, Kilcoyne D, Berrah N and Rolles D 2019 A coincidence velocity map imaging spectrometer for ions and high-energy electrons to study inner-shell photoionization of gas-phase molecules *Rev. Sci. Instrum.* **90** 055103
[79] Bodi A, Hemberger P, Gerber T and Sztáray B 2012 A new double imaging velocity focusing coincidence experiment: i2PEPICO *Rev. Sci. Instrum.* **83** 083105
[80] Lehmann C S, Ram N B and Janssen M H M 2012 Velocity map photoelectron-photoion coincidence imaging on a single detector *Rev. Sci. Instrum.* **83** 093103
[81] Zhao A, Sándor P and Weinacht T 2017 Coincidence velocity map imaging using a single detector *J. Chem. Phys.* **147** 013922
[82] Fan L, Lee S K, Tu Y-J, Mignolet B, Couch D, Dorney K, Nguyen Q, Wooldridge L, Murnane M, Remacle F, Bernhard Schlegel H and Li W 2017 A new electron-ion coincidence 3D momentum-imaging method and its application in probing strong field dynamics of 2-phenylethyl-N, N-dimethylamine *J. Chem. Phys.* **147** 013920
[83] Arion T and Hergenhahn U 2015 Coincidence spectroscopy: Past, present and perspectives *J Electron Spectrosc* **200** 222-31
[84] Fan L, Lee S K, Chen P Y and Li W 2018 Observation of Nanosecond Hot Carrier Decay in Graphene *J. Phys. Chem. Lett.* **9** 1485-90
[85] Debrah D A, Stewart G A, Basnayake G, Tisch J W G, Lee S K and Li W 2019 Direct in-situ single-shot measurements of the absolute carrier-envelope phases of ultrashort pulses *Opt. Lett.* **44** 3582-5
[86] Poikela T, Plosila J, Westerlund T, Campbell M, Gaspari M D, Llopart X, Gromov V, Kluit R, Beuzekom M v, Zappon F, Zivkovic V, Brezina C, Desch K, Fu Y and Kruth A 2014 Timepix3: a 65K channel hybrid pixel readout chip with simultaneous ToA/ToT and sparse readout *J. Instrum.* **9** C05013-C
[87] Zhao A, van Beuzekom M, Bouwens B, Byelov D, Chakaberia I, Cheng C, Maddox E, Nomerotski A, Svihra P, Visser J, Vrba V and Weinacht T 2017 Coincidence velocity map imaging using Tpx3Cam, a time stamping optical camera with 1.5 ns timing resolution *Rev. Sci. Instrum.* **88** 113104
[88] Hirvonen L M, Fisher-Levine M, Suhling K and Nomerotski A 2017 Photon counting phosphorescence lifetime imaging with TimepixCam *Rev. Sci. Instrum.* **88** 013104

[89] Nomerotski A 2019 Imaging and time stamping of photons with nanosecond resolution in Timepix based optical cameras *Nucl Instrum Meth A* **937** 26-30
[90] Fan L, Lee S K, Chen P-Y and Li W 2018 Observation of Nanosecond Hot Carrier Decay in Graphene *J. Phys. Chem. Lett.* **9** 1485-90
[91] Lucchese R R and Stolow A 2012 Molecular-frame photoelectron angular distributions *J. Phys. B-At. Mol. Opt. Phys.* **45** 190201
[92] Eckle P, Smolarski M, Schlup P, Biegert J, Staudte A, Schoffler M, Muller H G, Dorner R and Keller U 2008 Attosecond Angular Streaking *Nat. Phys.* **4** 565-70
[93] Pfeiffer A N, Cirelli C, Smolarski M, Wang X, Eberly J H, Doerner R and Keller U 2011 Breakdown of the independent electron approximation in sequential double ionization *New J. Phys.* **13** 093008
[94] Smolarski M, Eckle P, Keller U and Dörner R 2010 Semiclassical model for attosecond angular streaking *Opt. Express* **18** 17640-50
[95] Holmegaard L, Hansen J L, Kalhoj L, Louise Kragh S, Stapelfeldt H, Filsinger F, Kupper J, Meijer G, Dimitrovski D, Abu-samha M, Martiny C P J and Bojer Madsen L 2010 Photoelectron angular distributions from strong-field ionization of oriented molecules *Nat. Phys.* **6** 428-32
[96] Akagi H, Otobe T, Staudte A, Shiner A, Turner F, Dörner R, Villeneuve D M and Corkum P B 2009 Laser Tunnel Ionization from Multiple Orbitals in HCl *Science* **325** 1364-7
[97] Winney A H, Basnayake G, Debrah D A, Lin Y F, Lee S K, Hoerner P, Liao Q, Schlegel H B and Li W 2018 Disentangling Strong-Field Multielectron Dynamics with Angular Streaking *J. Phys. Chem. Lett.* **9** 2539-45
[98] Krause P, Sonk J A and Schlegel H B 2014 Strong field ionization rates simulated with time-dependent configuration interaction and an absorbing potential *J. Chem. Phys.* **140** 174113
[99] Krause P and Schlegel H B 2015 Angle-Dependent Ionization of Small Molecules by Time-Dependent Configuration Interaction and an Absorbing Potential *J. Phys. Chem. Lett.* **6** 2140-6
[100] Hoerner P and Schlegel H B 2017 Angular Dependence of Strong Field Ionization of CH3X (X = F, Cl, Br, or I) Using Time-Dependent Configuration Interaction with an Absorbing Potential *J. Phys. Chem. A* **121** 5940-6
[101] Winney A H, Lee S K, Lin Y F, Liao Q, Adhikari P, Basnayake G, Schlegel H B and Li W 2017 Attosecond Electron Correlation Dynamics in Double Ionization of Benzene Probed with Two-Electron Angular Streaking *Phys. Rev. Lett.* **119** 123201
[102] Liao Q, Winney A H, Lee S K, Lin Y F, Adhikari P and Li W 2017 Coulomb-repulsion-assisted double ionization from doubly excited states of argon *Phys. Rev. A* **96** 023401
[103] Weeraratna C, Amarasinghe C, Lee S K, Li W and Suits A G 2018 Demonstration of multi-hit and multi-mass capability of 3D imaging in a conventional velocity map imaging experiment *J. Chem. Phys.* **149** 084202